To be resubmitted to Building and Environment 2020

Effects of urban geometry on thermal environment in 2D street canyons: A scaled experimental study

Guanwen Chen[1,2,3,#], Cho Kwong Charlie Lam[1,2,3,#], Kai Wang[4], Boguang Wang[5], Jian Hang[1,2,3,*], Qun Wang[4], Xuemei Wang[5]

[1]School of Atmospheric Sciences, Sun Yat-sen University, Zhuhai 519082, China

[2]Key Laboratory of Tropical Atmosphere-Ocean System, Ministry of Education, Zhuhai 519082, China

[3]Southern Marine Science and Engineering Guangdong Laboratory, Zhuhai 519082, China

[4]Department of Mechanical Engineering, the University of Hong Kong, Pok Fu lam Road, Hong Kong

[5]Institute for Environmental and Climate Research, Jinan University, Guangzhou, P. R. China

*Corresponding author: Jian Hang

Tel: +86-13710248541

E-mail address: hangj3@mail.sysu.edu.cn

#First authors: Guanwen Chen, Cho Kwong Charlie Lam

Abstract:

Changes in urban geometry significantly alters the urban microclimate. Suitable urban geometrical layouts can effectively improve the urban thermal environment to achieve a more sustainable and healthier city. A quantitative assessment of the relationship between the urban geometry and thermal environment is essential to provide scientific guidance for better urban and building design. Hence, we performed a scaled outdoor measurement to investigate the diurnal variations in air, and west and east wall temperatures within two-dimensional (2D) street canyons. We adopted the daily average temperature $\overline{T}$, daily temperature range *DTR*, and hottest time t_{max} to describe the diurnal temperature characteristics. The influence of aspect ratios was considered (building height/street width, *H/W*=0.5, *H*=0.5 m, and *H/W*=1, 2, 3, 6, *H*=1.2 m). Canyon air experienced a smaller $\overline{T}$ and *DTR* compared with the east and west walls. With an increase in the aspect ratio, no significant difference was observed in the $\overline{T}$ of canyon air. The east and west walls of *H/W*=2, 3, and 6 experienced lower $\overline{T}$ (26.1-26.9 ℃) and smaller *DTR* (11.7-18.4 ℃) than those of *H/W*=0.5, 1 ($\overline{T}$=26.7-28.7 ℃ and *DTR*=16.0-26.1 ℃). A higher phase lag of t_{max} occurred between *H/W*=0.5, and *H/W*=6. As the aspect ratio increased, the differences in $\overline{T}$, *DTR*, and t_{max} between the east and west walls decreased. This study improves our understanding of how urban morphology influences urban thermal environment and provides meaningful references for urban planning. Such high-quality experimental data can be used to validate and further improve numerical simulations and theoretical models.

Keywords: Street canyon, Aspect ratio, Street-wall orientation, Diurnal temperature cycle, Fast Fourier transform (FFT)

1. Introduction

Urbanization has resulted in a significant increase in tall and dense buildings and has modified the surface energy balance of urban areas [1]. This has led to the urban heat island (UHI) effect, in which the air/surface temperature of the urban area is higher than that of the surrounding rural area [2]. The UHI results in increased building energy consumption for cooling [3] and causes adverse effects on the outdoor thermal comfort [4] and human health [5]. Therefore, attention should be paid to the extra heat stress induced by the UHI.

In recent years, numerous studies have been conducted to understand the urban thermal environment and provide insightful mitigation strategies for the UHI effect in regulating the configurations of urban geometry [6], vegetation [7], reflective surfaces [8] and water bodies [9]. In particular, a suitable urban geometrical layout is found to be the most effective technique for improving the thermal environment in summer [10].

Previous studies have adopted the aspect ratio (*H/W*, the ratio of building height to street width) to define the urban geometry for two-dimensional (2D) street canyons [6]. A higher *H/W* value indicates a compact and dense urban space. Some researchers have investigated the impact of urban morphology on radiation [11], wind speed [12], thermal comfort [13], and surface and air temperature [14]. Urban geometry influences the thermal environment by modifying the convective and radiative heat transfer processes. As the aspect ratio increases, urban wind speed decreases [15], and the amount of incoming and outgoing radiation reduces [16]. This results in a non-linear relationship between the urban morphology and thermal environment owing to various counteracting processes. These processes include the convective effect of airflow, the shading effect of direct shortwave radiation, and the trapping effect of diffuse shortwave radiation and longwave radiation [17]. It is a challenge to determine an optimal canyon geometry for simultaneously improving the convective ventilation and maximizing the shelter effect of solar radiation [18]. Thus, further investigations are required to quantify the effects of urban geometry on the thermal environment.

Previous studies have proposed numerical simulations and observational approaches to investigate the diurnal cycle of an urban microclimate with various building configurations. The main advantage of numerical simulations is the ability to perform parametric analyses and provide high-resolution computational results. However, the idealized boundary conditions and simplified physical processes may cause simulation uncertainties resulting in compromised numerical accuracy. Therefore, further high-quality experimental data on the urban thermal environment are necessary to validate and improve numerical simulations [19].

Full-scale field experiments offer the possibility of investigating the urban airflow and thermal structure from real situations inside street canyons with various aspect ratios [20]. However, it is challenging to perform high-quality parametric observational studies in full-scale street canyons because of uncontrollable urban geometries and heterogeneous surface materials [21]. Furthermore, the measurements are usually limited with regard to spatial and temporal resolutions and are possibly affected by anthropogenic activities.

As a result, some scaled experimental studies with flexibly controlled urban geometrical layouts and building materials have been conducted in laboratories and outdoors. Among scaled experimental studies in laboratories, both wind tunnel [22] and water tank experiments [23] have examined the effect of urban morphology on urban airflows. However, the diurnal cycles of the urban thermal environment with heat storage and radiation processes are hardly realized in such scaled experimental models in laboratories.

Scaled outdoor experiments that satisfy thermodynamic similarity requirements [24] are verified as a good option to perform high-quality parametric observational studies under the same meteorological conditions. Previous studies have examined the basic features of surface energy balance [25], convective heat transfer [26], evaporative cooling [27], and thermal mitigation from urban vegetation [28] and water bodies [29]. Furthermore, some scaled outdoor measurements have been performed to evaluate the effects of urban geometry on urban albedo [30] and pedestrian energy exchange [31]. However, few scaled outdoor experiments have been conducted to investigate the diurnal patterns of urban thermal environment with various urban morphologies.

Therefore, in this study, we performed scaled outdoor measurements to examine the diurnal temperature characteristics in 2D street canyons and quantify the effects of urban morphology on the thermal environment. We measured air and wall temperature of different 2D street canyons (H/W = 0.5, H = 0.5 m; H/W = 1, 2, 3, 6, H = 1.2 m) in Scaled Outdoor Measurement of Urban Climate and Health (SOMUCH). In particular, this study answers the following research questions:

1）What are the diurnal characteristics of air temperature, east and west wall temperatures in 2D street canyons?

2）How does the above diurnal characteristics differ in 2D street canyons with various aspect ratios?

Understanding the temporal features of the surface and air temperature in urban areas is essential for studying the thermal environment. To better describe the diurnal characteristics, mean temperature, daily temperature range (DTR), and phase were adopted here, because an integrated study of changes in these parameters can provide more information to capture the dynamics of the urban thermal environment [32]. Understanding such characteristics of diurnal temperature cycles with various urban morphologies will help urban planners better design and improve the urban thermal environment. Moreover, high-quality experimental data can be used to validate and improve numerical simulations [33] and theoretical models [34] in future urban climate studies.

2. Methodology

2.1 Experimental setup

The SOMUCH experiment platform was located in the suburb of Guangzhou, P.R. China (23°1' N, 113°25' E). Our SOMUCH experiment satisfies both geometrical and dynamical similarities between the scaled model and the real world (see [35] for similarity analysis results). Dynamical similarity refers to the similarities with respect to air flow, radiation, and thermal inertia. Several SOMUCH experiments have been conducted to study the characteristics of interunit dispersion [36], and investigate the effects of thermal storage [35], buoyancy force [37], and urban vegetation [38] on the thermal environment and flow characteristics in 2D street canyons.

In this study, as shown in Fig. 1a-c, we used 1488 hollow concrete building models (wall thickness δ = 1.5 cm) to construct street canyons without anthropogenic influence on a 57 m × 57.5 m flat concrete base. The detailed physical properties of the concrete model used in this measurement are listed in Table 1. To mimic various urban morphologies, five different aspect ratios (building height/street width, H/W) were considered: H/W = 0.5 (H = 0.5 m) and H/W = 1, 2, 3, and 6 (H = 1.2 m). Each aspect ratio contains six street canyons (except four street canyons for H/W = 6), and the length of each street canyon is L = 12 m (except L = 33.6 m for H/W = 0.5). As depicted in Fig. 1a-b, the street canyon axis is oriented at $-25°$ with respect to the north. The cross-canyon direction corresponds to X, the along-canyon direction is defined as Y, and the vertical direction is Z. Furthermore, Fig. 1c shows the definitions of the canyon air, ground, west wall, and east wall in 2D street canyons.

Measurements were simultaneously conducted from July 30 to December 15, 2019. During the experimental period, weather stations (RainWise PortLog), CMP10 (Kipp & Zonen), and CGR3 (Kipp & Zonen) were used to measure the atmospheric background conditions. Furthermore, sonic anemometers (Gill WindMaster), and thermocouples (Omega, TT-K-30-SLE, Φ0.255 mm and TT-K-36-SLE, Φ0.127 mm) were applied to measure the three wind velocity components (u, v, w), surface and air temperature within street canyons, respectively. The detailed configurations and specifications of the instrumentation used in the present study are provided in Table 2, Fig. 1b (top view), Fig. 2a-b, Fig. 3a-c, Fig. 4, and Fig. 5 (side view).

As depicted in Fig. 1b, two weather stations (RainWise PortLog) were used to measure the background air temperature, rainfall, and relative humidity. The sensors of the weather stations were set at a height of 2.4 m (i.e., $z = 2H$) above the ground, and their monitoring time interval was 5 min. Additionally, we used the CMP10 (Kipp & Zonen, z = 1.3 m) and CGR3 (Kipp & Zonen, z = 1.9 m) to measure the global solar radiation and downward longwave radiation on a horizontal surface at intervals of 1 s.

As displayed in Fig. 2a-b, 200 thermocouples (Omega, TT-K-30-SLE, Φ0.255 mm) with radiation shield were applied to measure the west and east wall temperatures inside street canyons with various aspect ratios (H/W = 0.5, H = 0.5 m; H/W = 1, 2, 3, 6, H = 1.2 m). The measurement points at the west wall (20 thermocouples) and east wall (20 thermocouples) were arranged in a regular grid consisting of five vertical heights and four horizontal positions in each street canyon of H/W = 0.5 (Fig. 2a), and H/W = 1, 2, 3, and 6 (Fig. 2b). These temperature data were recorded by Agilent 34972A data loggers at a frequency of 3 s.

Fig. 3a-c show that 198 bare thermocouples (Omega, TT-K-36-SLE, Φ0.127 mm) logged by Agilent 34972A at intervals of 3 s were placed to measure the air temperature in the cross-section of the street canyons (H/W = 0.5, H = 0.5 m; H/W = 1, 2, 3, 6, H =

1.2 m). The effect of solar radiation on such fine thermocouples without radiation shield could be neglected [29]. For $H/W = 0.5$ (Fig. 3a) and $H/W = 1, 2, 3$ (Fig. 3b), a total number of 42 thermocouples stuck to the nylon wires (Φ0.66 mm) were installed in a reticular formation (six vertical heights, seven horizontal positions) in each street canyon. Due to the limited space in street canyons with $H/W = 6$ ($W = 0.2$ m) (Fig. 3c), thirty thermocouples attached to the nylon wires were set up in a grid composed of six horizontal levels and five vertical lines. To prevent the thermocouples stuck in nylon wires from moving in the wind, the upper part of the nylon wires was fixed on the steel rope (Φ1.21 mm), and the bottom of the nylon wires was screwed into the ground. Furthermore, the arrangement of thermocouples in each horizontal level was uneven, and the temperature sensors were densely distributed near the wall surface (the closest distance was 0.02 m). Such high-resolution configurations of thermocouples are usually difficult to install in real cities [39]. Furthermore, as shown in Fig. 4, 21 thermocouples (Omega, TT-K-36-SLE, Φ0.127 mm) were applied to measure the ground temperature in the cross-section of the street canyons ($H/W = 1, 2, 3$, $H = 1.2$ m). The measurement points at the ground were also arranged closely to the wall surface.

Fig. 5 displays that six sonic anemometers (Gill WindMaster) were horizontally instrumented at two different heights ($z = 0.3$ m, 2.4 m) in street canyons of $H/W = 1$, 2, 3. They were set up nearly in the central part (0.46L; $L = 12$ m) of the street canyon. Wind velocity components in cross-canyon direction u, along-canyon direction v and vertical direction w were measured at a frequency of 20 Hz.

2.2 Data analysis method

This study selected the recorded data from July 30–December 15, 2019, without rainfall and missing values. These data were used to investigate the influences of aspect ratios (*H/W* = 0.5, 1, 2, 3, and 6) on the diurnal cycle characteristics of air and west and east wall temperatures in 2D street canyons.

For temperature analysis, $\overline{T}$ represents the temporally averaged temperature for 10 min or one day (if not specified, the temperature data were averaged for 10 min), and $\langle T \rangle$ denotes the spatially averaged temperature at various points. To better visualize the thermal structure inside street canyons, the 10 min averaged temperature of canyon air ($\overline{T}_{air}$), west wall ($\overline{T}_{west\ wall}$), and east wall ($\overline{T}_{east\ wall}$) measured by thermocouples on a typical day were linearly interpolated to a uniformly finer grid based on the present configurations of thermocouples (Fig. 2a-b and Fig. 3a-c) [39]. Then, some examples of diurnal variations of $\overline{T}_{air}$, $\overline{T}_{west\ wall}$, and $\overline{T}_{east\ wall}$ in street canyons with various aspect ratios (*H/W* = 0.5, 1, 2, 3, 6) were analyzed. Moreover, we evaluated the ventilation efficiency of street canyons by comparing the 10 min averaged wind velocity magnitude $V = \sqrt{u^2 + v^2 + w^2}$ for *H/W* = 1, 2, 3. Based on such temperature distribution and wind flow characteristics, we further analyzed the net radiation, sensible heat flux, and heat storage flux of the canyon wall. The detailed calculations of the heat fluxes were provided in Appendix A.

For long-term temperature data analysis, we applied the fast Fourier transform (FFT) method to convert temperature variations into a set of harmonics [40]. Daily (24 h) and semi-daily (12 h) harmonics, as well as the mean temperature, can adequately describe the diurnal temperature variations (i.e., $T_d(t)$, t denotes 0 to 24 h), as shown in Eq. (1):

$$T_d(t) = \bar{T} + \Delta\tilde{T}_{d1}\cos\left(\frac{2\pi}{day}t - \Phi_{d1}\right) + \Delta\tilde{T}_{d2}\cos\left(\frac{2\pi}{(day/2)}t - \Phi_{d2}\right), \quad (1)$$

where $\bar{T}$ is the mean temperature, $\Delta\tilde{T}_{d1}\cos\left(\frac{2\pi}{day}t - \Phi_{d1}\right)$ is the daily (24 h) harmonic with amplitude $\Delta\tilde{T}_{d1}$ and phase Φ_{d1}, $\Delta\tilde{T}_{d2}\cos\left(\frac{2\pi}{(day/2)}t - \Phi_{d2}\right)$ is the semi-daily (12 h) harmonic with amplitude $\Delta\tilde{T}_{d2}$ and phase Φ_{d2}.

First, the 10 min averaged temperature of all points measured by thermocouples during July 30–December 15, 2019, were selected as input data for FFT analysis. We then obtained the daily temperature variations $T_d(t)$ (expressed in Eq. (1)) of each measured point in canyon air, west wall, and east wall inside street canyons with various aspect ratios (*H/W* = 0.5, 1, 2, 3, 6). To better understand the phase, the warmest time of the day was used to describe the phase [41]. Based on $T_d(t)$, we further calculated the diurnal temperature characteristics in terms of daily average temperature ($\bar{T}$), daily temperature range (*DTR*), and hottest time (t_{max}). In detail, $\bar{T}$ was computed as the mean temperature during the entire day, *DTR* was calculated as the difference between daily maximum temperature and daily minimum temperature, and t_{max} corresponded to the occurrence time of the daily maximum temperature. In order to present more representative patterns of diurnal temperature, we further computed the spatially averaged values with standard deviations of $T_d(t)$, $\bar{T}$, *DTR*, and t_{max} at all corresponding points in the canyon air and west and east walls. Finally, such diurnal temperature characteristics were adopted to quantify the effects of aspect ratios (*H/W* = 0.5, 1, 2, 3, 6) and street-wall orientation (the orientation of a street canyon wall) on the thermal environment of 2D street canyons.

3. Results

3.1 Typical diurnal cycle of urban thermal environment

The daily cycle of the urban thermal environment was observed using our SOMUCH platform. As an example, Fig. 6a-c show the diurnal variations of the linearly interpolated temperature of the west wall ($\overline{T}_{west\ wall}$, Fig. 6a), east wall ($\overline{T}_{east\ wall}$, Fig. 6b), and canyon air ($\overline{T}_{air}$, Fig. 6c) measured by thermocouples within a street canyon of *H/W* = 3 on a typical day (November 4, 2019).

For wall temperature (as shown in Fig. 6a-b), owing to the enhanced solar radiation, both the $\overline{T}_{west\ wall}$ (Fig. 6a) and $\overline{T}_{east\ wall}$ (Fig. 6b) experience higher values during the daytime, especially in the afternoon. In addition, $\overline{T}_{west\ wall}$ and $\overline{T}_{east\ wall}$ of the upper levels are higher than those of the lower levels, indicating that a stronger temperature gradient appears in the vertical direction as upper levels receive more solar radiation with less shading area than the lower levels.

However, the $\overline{T}_{west\ wall}$ and $\overline{T}_{east\ wall}$ attain much lower values at night owing to longwave radiation loss and convective cooling. Furthermore, the vertical temperature gradients of the $\overline{T}_{west\ wall}$ and $\overline{T}_{east\ wall}$ become much lesser. Such linearly interpolated wall temperature distribution measured by thermocouples shows similar daily cycle phenomena with the observations captured by infrared cameras [35].

For canyon air temperature (as displayed in Fig. 6c), the values of $\overline{T}_{air}$ are markedly lesser than those of the $\overline{T}_{west\ wall}$ (Fig. 6a) and the $\overline{T}_{east\ wall}$ (Fig. 6b) during the daytime. In addition, a higher $\bar{T}_{air}$ occurs in the region closer to the heated wall. In the present study, the west wall is heated up firstly in the morning (e.g., higher $\bar{T}_{air}$ appears in the near region of the west wall at 10:00), while the east wall presents a higher temperature in the afternoon, especially at the upper levels (e.g., higher $\bar{T}_{air}$ is located in the closer area of the east wall at 15:00).

3.2 Impact of street-wall orientation on typical wall temperature

Street-wall orientation is an important factor that affects solar access and wall temperature. Fig. 7a-b display examples of diurnal variations (e.g., November 4, 2019) of the linearly interpolated temperature of the west wall ($\bar{T}_{west\ wall}$) and the east wall ($\bar{T}_{east\ wall}$) measured by thermocouples within a street canyon of *H/W* = 2.

As depicted in Fig. 7a, during the daytime, first the west wall is exposed to direct solar radiation; and the $\bar{T}_{west\ wall}$ increases earlier in the morning, while the east wall receives direct solar radiation in the afternoon; thus increasing $\bar{T}_{east\ wall}$. However, at night (Fig. 7b), the temperature difference between the east and west walls becomes lesser owing to the absence of solar radiation. Such phenomena are generally consistent with observations in realistic street canyons [42].

3.3 Impact of aspect ratio on typical urban thermal environment

The aspect ratio (building height/street width, *H/W*) can be used to characterize the building density and urban compactness in 2D street canyons (i.e., higher aspect ratios correspond to narrower street canyons), which play a significant role in the urban thermal environment by changing both ventilation and radiation. As the aspect ratio increases, street ventilation worsens [43], and less surface area within the street canyon is exposed to direct solar radiation [44].

3.3.1 Analysis of wind speed

Fig. 8 shows the diurnal cycle (e.g., November 4, 2019) of 10 min averaged wind velocity magnitude $\overline{V}$ and its standard deviation at two heights (z = 0.3 m, 2.4 m) inside street canyons with different aspect ratios (*H*/*W* = 1, 2, 3). For street canyons of all aspect ratios, the wind speeds at z = 0.25*H* are significantly lesser than those at z = 2*H*. Furthermore, the mean value of $\overline{V}_{0.25H}$ during the entire day is 0.837 m/s, 0.735 m/s, and 0.354 m/s for *H*/*W* = 1, 2, and 3, respectively. This indicates that narrower street canyons experience worse ventilation effects.

However, the relatively large standard deviations (as shown in the colored strips in Fig. 8) may affect the presented results. We also applied a linear regression method to estimate the relationship between $V_{0.25H}$ and V_{2H} from July 30–December 15, 2019. Then, the normalized velocity magnitude $V_{0.25H}/V_{2H}$ can be used to evaluate the ventilation efficiency of street canyons [28]. Table 3 summarizes $V_{0.25H}/V_{2H}$ in street canyons with *H*/*W* = 1, 2, and 3 during the entire experimental period. $V_{0.25H}/V_{2H}$ of *H*/*W* = 1 ($V_{0.25H}/V_{2H}$= 0.41) is higher than that of *H*/*W* = 2 ($V_{0.25H}/V_{2H}$= 0.36) and *H*/*W* = 3 ($V_{0.25H}/V_{2H}$= 0.21). Such long-term flow characteristics also suggest that poor ventilation occurs in narrower streets.

3.3.2 Analysis of wall temperature

Fig. 9a-b display examples of diurnal cycles (e.g., November 4, 2019) of linearly interpolated wall temperature (e.g., $\overline{T}_{east\ wall}$) distribution measured by thermocouples in street canyons with five different aspect ratios (*H/W* = 0.5, 1, 2, 3, 6). During the daytime (Fig. 9a), the lower regions of $\overline{T}_{east\ wall}$ in narrower street canyons are lesser due to the greater shading effect, especially in *H/W* = 6. However, at night (Fig. 9b), the lower levels of narrower street canyons (e.g., *H/W* = 6) attain higher temperature because of worse ventilation and less longwave radiation loss.

3.3.3 Analysis of canyon air temperature

Fig. 9c-d show examples of diurnal cycles (e.g., November 4, 2019) of linearly interpolated air temperature ($\overline{T}_{air}$) distribution measured by thermocouples in street canyons with different aspect ratios (*H/W* = 0.5, 1, 2, 3, 6). The air temperature distribution within the street canyon was significantly affected by wall surface heating. As shown in Fig. 9c, during the daytime, a higher $\overline{T}_{air}$ that is closer to the heated wall can be observed in all street canyons (*H/W* = 0.5, 1, 2, 3, 6). Furthermore, a higher $\overline{T}_{air}$ could be obtained in wider street canyons (*H/W* = 0.5, 1) near the ground level, whereas a higher $\overline{T}_{air}$ is mostly located in the upper levels of narrower street canyons (e.g., *H/W* = 6) because of the lesser wall temperature of the lower regions.

However, at night (Fig. 9d), $\overline{T}_{air}$ becomes much more uniform inside the street canyons. In addition, the $\overline{T}_{air}$ of wider street canyons (*H/W* = 0.5, 1) decreases faster than those of narrower street canyons (e.g., *H/W* = 6) because the wider street canyons attain stronger turbulent mixing and better ventilation.

3.3.4 Analysis of heat fluxes

Fig. 10 presents the diurnal variations (e.g. November 4, 2019) of 10 min averaged net radiation Q^* (Fig. 10a), heat storage flux ΔQ_s (Fig. 10b), and sensible heat flux Q_H (Fig. 10c) of the east wall in street canyons of *H/W* = 1, 2, and 3. The detailed estimations of the heat fluxes can be seen in Appendix A.

During the daytime, the Q^* of the east wall reaches a first peak in the morning, and a second maximum value in the afternoon. The second peak value is higher due to the east wall receives direct solar radiation in the afternoon, while the first peak is mainly affected by the reflected radiation from the west wall. Such phenomena are in agreement with the observations reported by Nunez and Oke [45]. In general, the east wall of wider street canyon (*H/W* = 1) attains higher Q^*, smaller ΔQ_s and larger Q_H than those of narrower street canyons (*H/W* = 2, 3). There is less shading effect in the wider street canyon, daytime Q^* is much higher, which would result a higher surface temperature. Together with the stronger wind, the convective sensible heat flux is much larger. At the same time, the heat storage flux ΔQ_s is smaller in the wider street canyon.

At night, owing to the absence of solar input, longwave radiative cooling dominates the $Q^*$of the east wall ($Q^* < 0$). And the magnitude of Q^* in narrower street canyon is relatively smaller due to the increased longwave trapping effect. The stored heat on the east wall is released ($\Delta Q_s < 0$). Due to the decreased wall-air temperature differences, the value of Q_H becomes much smaller at night compared with those during the daytime. Moreover, the differences of Q^*, ΔQ_s and Q_H between H/W = 1, 2, 3 are much lesser at night.

However, the estimated heat fluxes of the east wall cannot satisfy the energy balance closure. Such energy imbalance is probably due to the simplified heat flux parameterization and the limited spatial resolution of the measurement points. Table 4 further summarizes the differences between the Q_H and $Q_{H_{res}}$ (if the energy balance is satisfied, $Q_{H_{res}} = Q^* - \Delta Q_s$). The root mean squared error (RMSE) is 60.7 W/m^2, 32.4 W/m^2, and 23.0 W/m^2 for H/W = 1, 2, and 3, respectively.

3.4 Diurnal temperature variation obtained from long-term measurement

3.4.1 Effect of aspect ratio on the diurnal temperature cycle

Fig. 11a-c present the spatially averaged values of diurnal temperature obtained from FFT at all corresponding points of the west wall ($\langle T_{west\,wall} \rangle$), east wall ($\langle T_{east\,wall} \rangle$), and canyon air ($\langle T_{air} \rangle$) inside street canyons with various aspect ratios (H/W = 0.5, 1, 2, 3, 6).

For wall temperature (Fig. 11a-b), taking $\langle T_{west\,wall} \rangle$ (Fig. 11a) as an example, wider street canyons (e.g., H/W = 0.5, 1) with a more directly irradiated surface warm up faster and attain a higher $\langle T_{west\,wall} \rangle$ than narrower street canyons (e.g., H/W = 2, 3, 6) during the daytime. However, at night, $\langle T_{west\,wall} \rangle$ of wider street canyons (e.g., H/W = 0.5, 1) decreases faster because of better ventilation and greater longwave radiation loss. During the entire day, the largest west-wall temperature difference occurs in the street canyons of H/W = 0.5, and H/W = 6. Similar phenomena can be observed in $\langle T_{east\,wall} \rangle$ (Fig. 11b).

For canyon air temperature (as shown in Fig. 11c), during the daytime, $\langle T_{air} \rangle$ of the narrowest street canyon (i.e., *H/W* = 6) experiences lesser values owing to the weaker sensible heat transfer processes caused by lower surface temperature and significantly reduced wind speed inside the street canyon. Furthermore, it is difficult for the warm air above the roof to reach the lower portions of narrower street canyons because of the skimming flow patterns. However, at night, the widest street canyon (i.e., *H/W* = 0.5) attains a lower $\langle T_{air} \rangle$ because of the lesser surface heating and stronger turbulent mixing of air within and above street canyons. Similar observations have been reported by Johansson [46] in realistic street canyons of *H/W* = 0.6 and *H/W* = 9.7.

Moreover, during the entire day, the largest air temperature difference appears in the case of *H/W* = 0.5, and *H/W* = 6, while such differences among *H/W* = 1, 2, and 3 are much lesser, which is different from the cases of east and west wall temperatures. The results indicate that canyon air experiences more complex heat transfer mechanisms than the wall surface [47].

3.4.2 Effect of street-wall orientation on diurnal temperature cycle

Fig. 12 shows the spatially averaged values of diurnal temperature obtained from FFT at all corresponding points of the west wall ($\langle T_{west\,wall} \rangle$) and the east wall ($\langle T_{east\,wall} \rangle$) inside street canyons with various aspect ratios (*H/W* = 0.5, 1, 2, 3, 6).

For street canyons with all aspect ratios during the daytime, it can be observed that there are obvious phase lags between $\langle T_{west\,wall} \rangle$ and $\langle T_{east\,wall} \rangle$. $\langle T_{west\,wall} \rangle$

increases faster and reaches a peak value earlier than $\langle T_{east\ wall} \rangle$. However, $\langle T_{east\ wall} \rangle$ presents higher maximum values than $\langle T_{west\ wall} \rangle$ because of the greater solar loading of the east wall. In addition, as the aspect ratio increases, the maximum temperature difference between $\langle T_{east\ wall} \rangle$ and $\langle T_{west\ wall} \rangle$ decreases.

3.5 Analysis of diurnal cycle characteristics (daily average temperature, *DTR* and hottest time)

To quantify the diurnal cycle variations of the urban thermal environment, the daily average temperature ($\overline{T}$), daily temperature range (*DTR*), and hottest time (t_{max}) are calculated using the diurnal temperature expressions obtained from the FFT method. Fig. 13a-c display the spatially averaged values with standard deviations of diurnal temperature characteristics at all corresponding points of canyon air and east and west walls in street canyons with various aspect ratios (*H/W* = 0.5, 1, 2, 3, 6), and Table 5 summarizes the calculated results.

3.5.1 Daily average temperature $\overline{T}$

As shown in Fig. 13a and Table 5, for street canyons with the same aspect ratio, both $\overline{T}_{east\ wall}$ and $\overline{T}_{west\ wall}$ are higher than $\overline{T}_{air}$. For instance, $\overline{T}_{air}$ is 24.3 °C in the street canyon with *H/W* = 0.5, whereas $\overline{T}_{west\ wall}$ is 27.9 °C and $\overline{T}_{east\ wall}$ is 28.7 °C.

As the aspect ratio increases, the directly irradiated canyon surface area decreases. For wall temperature, $\overline{T}_{west\ wall}$ and $\overline{T}_{east\ wall}$ of wider street canyons (*H/W* = 0.5,

1) are higher than those of narrower street canyons (*H/W* = 2, 3, 6). In addition, east walls with greater solar loading experience higher $\overline{T}$ values than the west walls (except for *H/W* = 6). With an increase in the aspect ratio, the magnitude of differences in $\overline{T}$ between east and west walls becomes smaller (i.e., 0.8 °C, 0.8 °C, 0.5 °C, 0.5 °C, and 0.3 °C for *H/W* = 0.5, 1, 2, 3, and 6, respectively).

In contrast to the cases of $\overline{T}_{west\ wall}$ and $\overline{T}_{east\ wall}$, there is no significant difference in $\overline{T}_{air}$ among various aspect ratios (i.e., 24.3 °C, 24.2 °C, 24.3 °C, 24.5 °C, and 24.6 °C for *H/W* = 0.5, 1, 2, 3, and 6, respectively).

3.5.2 Daily temperature range (*DTR*)

As displayed in Fig. 13b and Table 5, the *DTRs* of the west and east walls are much higher than those of canyon air. As an example of a street canyon with *H/W* = 0.5, the *DTR* of canyon air is the smallest (10.9 °C), which is 7.6 °C and 15.2 °C lesser than that of the west wall and east wall, respectively.

Furthermore, the *DTR* of the west and east walls decline with an increase in the aspect ratio. For west wall, the *DTR* is 18.5 °C, 16.0 °C, 14.6 °C, 13.8 °C, and 11.7 °C for *H/W* = 0.5, 1, 2, 3, and 6, respectively. In the case of the east wall, the *DTR* of *H/W* = 0.5 is 26.1 °C, which is 3.3 °C, 7.7 °C, 9.6 °C, and 13.2 °C higher than for *H/W* = 1, 2, 3, and 6, respectively. We observe this result because wider street canyons receive more direct solar radiation, resulting in higher maximum temperatures during the daytime. Such street canyons with stronger longwave radiative cooling also experience lower minimum temperatures at night, producing greater *DTR* in wider street canyons.

Moreover, the east walls with greater solar loading exhibit a higher *DTR* than the west walls. However, as the aspect ratio increases, the *DTR* differences between east and west walls decrease (i.e., 7.6 °C, 6.8 °C, 3.8 °C, 2.7 °C, and 1.2 °C for *H/W* = 0.5, 1, 2, 3, and 6, respectively).

Compared with the cases of the east and west walls, the differences in the *DTR* of canyon air among various aspect ratios are much smaller. For canyon air, the *DTR* of *H/W* = 0.5 is 10.9 °C, which is 0.5 °C, 0.6 °C, 0.6 °C, and 1.6 °C higher than for *H/W* = 1, 2, 3, and 6, respectively.

3.5.3 Hottest time t_{max}

As depicted in Fig. 13c and Table 5, for street canyons with all aspect ratios, t_{max} on the east walls appears later than the west walls. This phenomenon occurs because the east wall absorbs direct solar radiation later than the west wall. The east wall with greater solar loading has more time to be heated (i.e., the appearance of maximum east wall temperature occurs later). Taking the street canyon of *H/W* = 0.5, as an example, t_{max} of the west wall occurs at 13.13 h, that of the east wall appears at 14.17 h.

Moreover, it seems that narrower street canyons with less solar loading experience later t_{max}. For wider street canyons, such as *H/W* = 0.5, t_{max} of canyon air, west wall, and east wall are 13.85 h, 13.13 h, and 14.17 h, respectively. For narrower street canyons, such as *H/W* = 6, t_{max} of canyon air, west wall, and east wall are 14.25 h, 14.85 h and 15.09 h, respectively. There is a considerably larger phase lag of t_{max} between *H/W* = 0.5 and *H/W* = 6 (i.e., 0.40 h, 1.72 h, and 0.92 h delay for canyon air, west wall, and east wall, respectively).

However, the differences in t_{max} of canyon air, west wall, and east wall for *H/W* = 1, 2, and 3 are much smaller. The maximum difference of t_{max} between *H/W* = 1, 2, and 3 is 0.03 h, 0.32 h, and 0.15 h for canyon air, west wall, and east wall, respectively. In addition, as the aspect ratio increases, the differences in t_{max} between the west and east walls become smaller, i.e., 1.04 h, 0.51 h, 0.29 h, 0.17 h, and 0.24 h for *H/W* = 0.5, 1, 2, 3, and 6, respectively.

4. Discussion

This study uses FFT in a scaled outdoor experiment, which distinguishes the daily mean temperature, diurnal temperature range, and hottest time in the temperature cycles from high-quality observational data. Our experimental results quantify the effects of urban morphology on the diurnal patterns of the thermal environment. In particular, not all the daily cycle characteristics of canyon air and east and west wall temperatures vary linearly with an increase in the aspect ratio.

The current study found no significant difference in the daily mean temperature of canyon air among the various aspect ratios. However, the decreases in *DTR* and the delay in the hottest time with increasing aspect ratio were clearer. This indicates that the *DTR* and hottest time (i.e., phase) should not be ignored when studying the effects of urban morphology on the thermal environment [41]. This phenomenon further verifies that the controlling factors for *DTR* and daily mean temperature are independent [40]. The decrease in *DTR* is mainly due to the increase in heat storage.

The rise in daily mean temperature is mainly related to the increased heat again, such as lesser albedo, more anthropogenic heat, and decreased latent cooling from the green area. As there is no anthropogenic heat or green area in our current model, the difference in daily mean temperature between various aspect ratios is very subtle.

Compared with the canyon air, the diurnal temperature characteristics of the east and west walls varied more significantly with the aspect ratio. Furthermore, the differences in diurnal temperature characteristics between the east and west walls became lesser as the aspect ratio increased. This suggests that multiple radiation exchanges may increase in the narrower street canyon [48], and thus, the temperature differences between the canyon surfaces are reduced.

Such simplified urban models are verified as a good option to study the thermal patterns of street canyons under realistic meteorological conditions. As urban morphology has been identified as a significant factor in building energy consumption [49], our quantitative research results can provide meaningful references for urban planners.

Our experimental study focuses on the effects of aspect ratios on radiation, wind flow and thermal storage in 2D street canyons. Only data obtained on specific days without rainfall was analyzed. There were no vegetation and water bodies inside the street canyons. The effects of latent heat flux on the thermal environment could be negligible in our study. However, it is quite worthwhile to study the latent heat flux, as we need to consider the effects of urban vegetation and water bodies on thermal environment in urban areas. The performance of urban surface energy balance models are still inadequate in predicting the latent heat flux [50]. Further high-quality experimental data are necessary to validate and improve such numerical models with latent heat flux. Urban vegetation study in our SOMUCH is in progress. We have investigated the influences of tree planting on the temperature and wind flow characteristics [38]. The impacts of urban vegetation on latent heat flux in 2D street canyons and 3D urban models will be emphasized in future experiments.

Understanding heat transfer processes is essential for studying the urban thermal environment. However, this study could not provide an accurate analysis of the heat transfer processes owing to the limited spatial measurement points. Further studies should be combined with numerical simulations such as the Computational Fluid Dynamics (CFD) models, to provide high-resolution computed results. Most numerical models rely on highly idealized assumptions, such as constant inlet boundary conditions [51]. More studies on the thermal environment in 2D street canyons and 3D urban districts are still required to perform unsteady numerical simulations and theoretical models with realistic meteorological forcing. Our study can provide high-quality parametric experimental data to validate and improve unsteady numerical simulations and theoretical models. Further attention should also be paid to quantify the relative role of the energy processes involved in 2D street canyons and 3D urban districts. These processes are vital for understanding the heat transfer mechanisms within urban areas and provide meaningful references for designing a comfortable urban thermal environment.

5. Conclusion

We performed a scaled outdoor field measurement to investigate the daily variations of air, west and east wall temperature within 2D street canyons (*H/W* = 0.5, *H* = 0.5 m; *H/W* = 1, 2, 3, 6, *H* = 1.2 m) during July 30–December 15, 2019. The fast Fourier transform (FFT) method was applied to obtain more generalized characteristics of diurnal temperature cycles (i.e., daily average temperature $\overline{T}$, daily temperature range DTR, and hottest time t_{max}), and further quantify the geometrical effects on the urban thermal environment.

Daily cycles of canyon air and east and west wall temperatures were observed, with higher values during the daytime and lesser values at night. During the daytime, the west and east wall temperatures experienced greater values than those of the canyon air. In addition, a stronger wall temperature gradient appeared in the vertical direction of the building facades, whereas a higher air temperature gradient occurred in the region that was closer to the heated wall. However, at night, the spatial distributions of canyon air and east and west wall temperatures became much more uniform.

Street-wall orientation is a significant factor that affects the wall temperature distribution. During the daytime, the west wall temperature increased faster but presented lower maximum values than the east wall. However, at night, the temperature differences between the east and west walls became much lesser. As a result, east walls with greater solar loading exhibited higher $\overline{T}$ (except for the street canyon of *H/W* = 6), larger DTR, and later t_{max} than the west walls.

The aspect ratio largely determines the thermal structures inside the street canyons.

Wider street canyons with less shaded areas usually attained higher wall and air temperatures during the daytime. However, they experienced lesser values at night because of the greater longwave radiative loss and more substantial convective cooling. Thus, the west and east walls of wider street canyons (*H/W* = 0.5, 1) exhibited higher $\overline{T}$ and larger *DTR* than narrower street canyons (*H/W* = 2, 3, 6). In contrast to the daily characteristics of the west and east wall temperatures, canyon air experienced a lower $\overline{T}$ and lesser *DTR*. With increasing aspect ratio, the *DTR* of canyon air decreased from 10.9 ℃ to 9.3 ℃ (i.e., 10.9℃, 10.4 ℃, 10.3 ℃, 10.3 ℃, and 9.3 ℃ for *H/W* = 0.5, 1, 2, 3, and 6, respectively). However, the $\overline{T}$ of canyon air remained nearly the same among various aspect ratios (i.e., 24.3 ℃, 24.2 ℃, 24.3 ℃, 24.5 ℃, and 24.6 ℃ for *H/W* = 0.5, 1, 2, 3, and 6, respectively).

Wider street canyons, such as *H/W* = 0.5, exhibited an earlier t_{max}. The higher phase lag of t_{max} occurred between *H/W* = 0.5 and *H/W* = 6 (i.e., 0.40 h, 1.72 h, and 0.92 h delayed for canyon air, west wall, and east wall, respectively). However, the maximum differences in t_{max} between street canyons with *H/W* = 1, 2, 3 were much lesser (i.e., 0.03 h, 0.32 h, and 0.15 h for canyon air, west wall, and east wall, respectively). Moreover, as the aspect ratio increased, the differences in $\overline{T}$, *DTR*, and t_{max} between the east and west walls became lesser.

Our results demonstrated that FFT is a useful approach for revealing the diurnal temperature characteristics of urban street canyons. By adopting the scaled model approach, we obtained the air and wall temperatures inside street canyons with a higher spatial distribution, which is otherwise difficult to observe in full-scale experiments.

Future urban climate studies can use high-quality experimental data to validate and improve numerical simulations and theoretical models, which can inform sustainable urban design.

Acknowledgements

This study was financially supported by the National Natural Science Foundation-Outstanding Youth Foundation (China, No. 41622502), National Natural Science Foundation of China (No. 41875015, No. 51811530017, No. 41905005), STINT (Sweden, dnr CH2017-7271), State Key Program of National Natural Science Foundation (China, No. 91644215), Key projects of Guangdong Natural Science Foundation (China, grant number 2018B030311068), Special Fund for Science and Technology Innovation Strategy of Guangdong Province (International cooperation) (China, No. 2019A050510021) and Innovation Group Project of Southern Marine Science and Engineering Guangdong Laboratory (Zhuhai) (No. 311020001).

Appendix A

To better understand the surface temperature distribution, it is essential to investigate the heat transfer processes of the canyon wall [52]. In this study, for instance, we analyzed the heat fluxes of the east wall, considering the incident shortwave radiation, multiple reflections of shortwave radiation with other surfaces, incoming longwave radiation, longwave radiation exchanges with other surfaces, heat storage flux, and convective heat transfer with the canyon air. We used the data obtained on specific days without rainfall. Furthermore, no vegetation and water bodies were set up in the street canyons. The latent heat flux was not considered here. The surface energy balance of east wall is expressed as Eq. (A1):

$$Q^* = S^* + L^* = \Delta Q_s + Q_H, \tag{A1}$$

where Q^* is the net radiation, S^* is the net shortwave radiation, L^* is the net longwave radiation, ΔQ_s is the heat storage flux, Q_H is the sensible heat flux.

A.1. Net radiation

We used radiation schemes from a single-layer urban canopy model [53]. Here, the subscripts *ew*, *ww*, and *g* denotes the east wall, west wall, and ground, respectively. It is assumed that the physical properties of the ground, east wall and west wall are the same in our SOMUCH experiments.

A.1.1 Net shortwave radiation

Three-time reflection of shortwave radiation was considered. We assumed that the surfaces are Lambertian, and the final reflected shortwave radiation is totally absorbed by each surface. The net shortwave radiation of east wall can be estimated as Eq. (A2):

$$S_{ew}^* = S_{ew}(1-\alpha_{ew}) + S_g\alpha_g\varphi_w(1-\alpha_{ew}) + S_{ww}\alpha_{ww}(1-2\varphi_w)(1-\alpha_{ew}) +$$
$$S_g\alpha_g\varphi_w\alpha_{ww}(1-2\varphi_w)(1-\alpha_{ew}) + S_{ew}\alpha_{ew}\frac{1}{2}(1-\varphi_g)\alpha_g\varphi_w(1-\alpha_{ew}) +$$
$$S_{ew}\alpha_{ew}(1-2\varphi_w)\alpha_{ww}(1-2\varphi_w)(1-\alpha_{ew}) + S_{ww}\alpha_{ww}\frac{1}{2}(1-\varphi_g)\alpha_g\varphi_w(1-$$
$$\alpha_{ew}) + S_g\alpha_g\varphi_w\alpha_{ew}\frac{1}{2}(1-\varphi_g)\alpha_g\varphi_w + S_g\alpha_g\varphi_w\alpha_{ew}(1-2\varphi_w)\alpha_{ww}(1-2\varphi_w) +$$
$$S_g\alpha_g\varphi_w\alpha_{ww}\frac{1}{2}(1-\varphi_g)\alpha_g\varphi_w + S_{ew}\alpha_{ew}\frac{1}{2}(1-\varphi_g)\alpha_g\varphi_w\alpha_{ww}(1-2\varphi_w) +$$

$S_{ew}\alpha_{ew}(1-2\varphi_w)\alpha_{ww}\frac{1}{2}(1-\varphi_g)\alpha_g\varphi_w + S_{ww}\alpha_{ww}\frac{1}{2}(1-\varphi_g)\alpha_g\varphi_w\alpha_{ww}(1-2\varphi_w) + S_{ww}\alpha_{ww}(1-2\varphi_w)\alpha_{ew}\frac{1}{2}(1-\varphi_g)\alpha_g\varphi_w + S_{ww}\alpha_{ww}(1-2\varphi_w)\alpha_{ew}(1-2\varphi_w)\alpha_{ww}(1-2\varphi_w)$, (A2)

where S_g, S_{ew}, and S_{ww} are the incident total shortwave radiation, α_g, α_{ew}, and α_{ww} are the albedo values (see Table 1, $\alpha = 0.24$), φ_g and φ_w are sky-view factors at the road and wall, respectively.

According to Sparrow and Cess [54], the sky-view factors are given by Eq. (A3-A4):

$$\varphi_g = (1 + (H/W)^2)^{1/2} - H/W, \tag{A3}$$

$$\varphi_w = \frac{1}{2}\{1 + H/W - [1 + (H/W)^2]^{1/2}\}/(H/W), \tag{A4}$$

where H is the building height, and W is the street width.

The total shortwave radiation incident on each surface is calculated using Eq. (A5-A7):

$$S_g = S_g^{direct} + \varphi_g S^{\downarrow diffuse}, \tag{A5}$$

$$S_{ew} = S_{ew}^{direct} + \varphi_w S^{\downarrow diffuse}, \tag{A6}$$

$$S_{ww} = S_{ww}^{direct} + \varphi_w S^{\downarrow diffuse}, \tag{A7}$$

where S_g^{direct}, S_{ew}^{direct} and S_{ww}^{direct} denotes the direct shortwave radiation incident on each surface, $S^{\downarrow diffuse}$ is the incoming diffuse shortwave radiation on a horizontal surface at the reference height ($S^{\downarrow diffuse}$ is assumed to be isotropic).

The direct shortwave radiation incident on each surface can be computed by Eq. (A8-A10):

$$S_g^{direct} = \begin{cases} S^{\downarrow direct}\left(1 - \frac{H}{W}\tan\emptyset_z|\sin\gamma|\right), for\ \frac{H}{W}\tan\emptyset_z|\sin\gamma| < 1 \\ 0,\ for\ \frac{H}{W}\tan\emptyset_z|\sin\gamma| \geq 1 \end{cases}, \quad (A8)$$

$$S_{sunlit\_w}^{direct} = \begin{cases} S^{\downarrow direct}\tan\emptyset_z|\sin\gamma|, for\ \frac{H}{W}\tan\emptyset_z|\sin\gamma| < 1 \\ S^{\downarrow direct}\frac{W}{H}, for\ \frac{H}{W}\tan\emptyset_z|\sin\gamma| \geq 1 \end{cases}, \quad (A9)$$

$$S_{shaded\_w}^{direct} = 0, \quad (A10)$$

where $S^{\downarrow direct}$ is the incoming direct shortwave radiation on a horizontal surface at the reference height, $S_{sunlit\_w}^{direct}$ and $S_{shaded\_w}^{direct}$ indicates the direct shortwave radiation for sunlit wall and shaded wall, respectively. $\emptyset_z$ is the solar zenith angle, γ (as shown in Eq. (A11)) is defined as the difference between the solar azimuth angle $\emptyset_a$ and the canyon orientation angle $\emptyset$. Both $\emptyset_a$ and $\emptyset$ are relative to the due north. When 0° ≤ γ ≤180° or γ ≤-180°, east wall is the sunlit wall.

$$\gamma = \emptyset_a - \emptyset, \quad (A11)$$

The solar zenith angle $\emptyset_z$ and solar azimuth angle $\emptyset_a$ can be calculated by Eq. (A12-A13):

$$\cos\emptyset_z = \cos\varphi_{lat}\cos\beta\cos\omega_t + \sin\varphi_{lat}\sin\beta, \quad (A12)$$

$$\cos\emptyset_a = (\cos\varphi_{lat}\sin\beta - \sin\varphi_{lat}\cos\beta\cos\omega_t)/\sin\emptyset_z, \quad (A13)$$

where φ_{lat} is the latitude, β is the solar declination angle, and ω_t is the hour angle.

The solar declination angle β is determined as Eq. (A14) [55]:

$$\beta = 23.45\sin(360\frac{284 + N}{365}), \quad (A14)$$

where N is the day number in the year.

The hour angle ω_t is given by Eq. (A15) [56]:

$$\omega_t = \pm 0.25\ \text{(Number of minutes from local solar noon)}, \quad (A15)$$

Following the algorithm proposed by Reindl et al. [57] (as shown in Eq. (A16-

A17)), we estimated the $S^{\downarrow direct}$ and $S^{\downarrow diffuse}$ on a horizontal surface based on the global solar radiation S_{global}.

$$S^{\downarrow diffuse} = \begin{cases} S_{global}[1 - 0.232k_t + 0.0239\sin\theta_s - 0.000682T_a + 0.0195RH], & for\ 0 \le k_t \le 0.3 \\ S_{global}[1.329 - 1.716k_t + 0.267\sin\theta_s - 0.00357T_a + 0.106RH], & for\ 0.3 < k_t < 0.78 \\ S_{global}[0.426k_t - 0.256\sin\theta_s + 0.00349T_a + 0.0734RH], & for\ k_t \ge 0.78 \end{cases}, \quad \text{(A16)}$$

$$S^{\downarrow direct} = \left(S_{global} - S^{\downarrow diffuse}\right)/\sin\theta_s, \quad \text{(A17)}$$

where θ_s is the solar altitude angle given by $\theta_s = 90° - \emptyset_z$ [56], k_t is the clearness index, T_a and RH are the background air temperature and relative humidity, respectively. Here, we used the measured values of S_{global} provided by CMP10, T_a and RH recorded by RainWise.

The clearness index k_t is defined in Eq. (A18) [56]:

$$k_t = S_{global}/I_0, \quad \text{(A18)}$$

where I_0 is the extraterrestrial radiation on a horizontal surface for an period between hour angles, ω_{t1} and ω_{t2} (ω_{t2} is larger). Its mathematical expression is shown in Eq. (A19) [56]:

$$I_0 = \frac{12\times3600G_{SC}}{\pi}\left[1 + 0.033\cos\left(\frac{360N}{365}\right)\right] \times \left\{\cos\varphi_{lat}\cos\beta(\sin\omega_{t2} - \sin\omega_{t1}) + \left[\frac{\pi(\omega_{t2}-\omega_{t1})}{180}\right]\sin\varphi_{lat}\sin\beta\right\}, \quad \text{(A19)}$$

in which G_{sc}=1367 W/m^2 is the solar constant.

A.1.2 Net longwave radiation

One-time reflection of longwave radiation was considered. We assumed that all longwave radiation is isotropic, and the last reflected longwave radiation is totally absorbed by each surface. The net longwave radiation of east wall can be calculated by Eq. (A20):

$$L_{ew}^{*} = L^{\downarrow}\varphi_w\varepsilon_{ew} + L_g\varphi_w\varepsilon_{ew} + L_{ww}(1-2\varphi_w)\varepsilon_{ew} + L^{\downarrow}\varphi_g(1-\varepsilon_g)\varphi_w + L^{\downarrow}\varphi_w(1-\varepsilon_{ww})(1-2\varphi_w) + L_g\varphi_w(1-\varepsilon_{ww})(1-2\varphi_w) + L_{ew}\frac{1}{2}(1-\varphi_g)(1-\varepsilon_g)\varphi_w + L_{ew}(1-2\varphi_w)(1-\varepsilon_{ww})(1-2\varphi_w) + L_{ww}\frac{1}{2}(1-\varphi_g)(1-\varepsilon_g)\varphi_w - L_{ew}, \quad \text{(A20)}$$

where $L^{\downarrow}$ is incoming longwave radiation on a horizontal surface at the reference height, ε_g, ε_{ew} and ε_{ww} are the surface emissivity (see Table 1, $\varepsilon =$ 0.87), L_g, L_{ww}, and L_{ew} are the emitted longwave radiation from surfaces. Here, we used the measured values of $L^{\downarrow}$ provided by CGR3.

Based on Stefan-Boltzmann law, the emitted longwave radiation from surface is calculated using Eq. (A21-A23):

$$L_g = \varepsilon_g\sigma T_g^4, \quad \text{(A21)}$$

$$L_{ww} = \varepsilon_{ww}\sigma T_{west\ wall}^4, \quad \text{(A22)}$$

$$L_{ew} = \varepsilon_{ew}\sigma T_{east\ wall}^4, \quad \text{(A23)}$$

where $\sigma = 5.67 \times 10^{-8}$ W/(m^{2}K^4) is the Stefan-Boltzmann constant, T_g, $T_{east\ wall}$, and $T_{west\ wall}$ are the temperatures (K) of the ground, east wall, and west wall, respectively. Here, the spatially averaged temperatures measured by thermocouples of the ground, east wall, and west wall were used.

A.2. Heat storage flux

We estimated the heat storage flux of the east wall using Eq. (A24) [58]:

$$\Delta Q_s = \frac{\Delta T}{\Delta t} C \Delta x \lambda_p , \tag{A24}$$

where $\Delta T/\Delta t$ is the rate of wall temperature change over the period, C = 1.496 $\mathrm{MJ}/(m^3K)$ is the volumetric heat capacity, Δx = 1.2 m is the height of the east wall, λ_p is the plan area density (i.e., plan area fraction of the east wall to the entire street canyon), and $\Delta x\lambda_p$ denotes the total volume of the east wall over the plan area. Here, the spatially average temperatures measured by thermocouples of the east wall were used to calculate the temperature change rate of 10 min. $\Delta x\lambda_p$ of the east wall is 0.0106, 0.0164, and 0.02 for H/W = 1, 2, and 3, respectively.

A.3. Sensible heat flux

The sensible heat exchange at the east wall can be expressed in Eq. (A25) [59]:

$$Q_H = h(T_{east\ wall} - T_{air}), \tag{A25}$$

where $T_{east\ wall}$ and T_{air} are the temperatures of the east wall and canyon air, respectively. The convective heat transfer coefficient (h) is calculated using Eq. (A26) [60]:

$$h = 11.8 + 4.2V, \tag{A26}$$

where $V = \sqrt{u^2 + v^2 + w^2}$ is the wind velocity magnitude within the street canyon.

Here, we used the spatially averaged temperatures measured by thermocouples of the east wall and canyon air. The wind velocity measured by sonic anemometers at z = 0.3 m = 0.25H (H = 1.2 m) was used to estimate h.

References

[1] Grimmond CSB, Roth M, Oke TR, Au YC, Best M, Betts R, Carmichael G, Cleugh H, Dabberdt W, Emmanuel R, Freitas E, Fortuniak K, Hanna S, Klein P, Kalkstein LS, Liu CH, Nickson A, Pearlmutter D, Sailor D, Voogt J. Climate and more sustainable cities: climate information for improved planning and management of cities (producers/capabilities perspective). Procedia Environmental Sciences, 2010, 1: 247-274.

[2] Oke TR, Mills G, Christen A, Voogt JA. Urban climates. Cambridge University Press, 2017.

[3] Li XM, Zhou YY, Yu S, Jia GS, Li HD, Li WL. Urban heat island impacts on building energy consumption: a review of approaches and findings. Energy, 2019, 174: 407-419.

[4] Jamei E, Rajagopalan P, Seyedmahmoudian M, Jamei Y. Review on the impact of urban geometry and pedestrian level greening on outdoor thermal comfort. Renewable and Sustainable Energy Reviews, 2016, 54: 1002-1017.

[5] Mora C, Dousset B, Caldwell IR, Powell FE, Geronimo RC, Bielecki CR, Counsell CW, Dietrich BS, Johnston ET, Louis LV, Lucas MP, McKenzie MM, Shea AG, Tseng H, Giambelluca T, Leon LR, Hawkins E, Trauernicht C. Global risk of deadly heat. Nature Climate Change, 2017, 7(7): 501-506.

[6] Chatzidimitriou A, Yannas S. Street canyon design and improvement potential for urban open spaces; the influence of canyon aspect ratio and orientation on

microclimate and outdoor comfort. Sustainable Cities and Society, 2017, 33: 85-101.

[7] Koc CB, Osmond P, Peters A. Evaluating the cooling effects of green infrastructure: a systematic review of methods, indicators and data sources. Solar Energy, 2018, 166: 486-508.

[8] Yang JC, Wang ZH, Kaloush KE. Environmental impacts of reflective materials: is high albedo a 'silver bullet' for mitigating urban heat island? Renewable and Sustainable Energy Reviews, 2015, 47: 830-843.

[9] Ampatzidis P, Kershaw T. A review of the impact of blue space on the urban microclimate. Science of the Total Environment, 2020,730: 139068.

[10] Lai DY, Liu WY, Gan TT, Liu KX, Chen QY. A review of mitigating strategies to improve the thermal environment and thermal comfort in urban outdoor spaces. Science of the Total Environment, 2019, 661: 337-353.

[11] Yang XY, Li YG. The impact of building density and building height heterogeneity on average urban albedo and street surface temperature. Building and Environment, 2015, 90: 146-156.

[12] Hang J, Xian ZN, Wang DY, Mak CM, Wang BM, Fan YF. The impacts of viaduct settings and street aspect ratios on personal intake fraction in three-dimensional urban-like geometries. Building and Environment, 2018, 143: 138-162.

[13] Li ZT, Zhang H, Wen CY, Yang AS, Juan YH. Effects of frontal area density on outdoor thermal comfort and air quality. Building and Environment, 2020, 180: 107028.

[14] Nazarian N, Kleissl J. CFD simulation of an idealized urban environment: thermal effects of geometrical characteristics and surface materials. Urban Climate, 2015, 12: 141-159.

[15] Yang HY, Chen TH, Lin YY, Buccolieri R, Mattsson M, Zhang M, Hang J, Wang Q. Integrated impacts of tree planting and street aspect ratios on CO dispersion and personal exposure in full-scale street canyons. Building and Environment, 2020, 169: 106529.

[16] Marciotto ER, Oliveira AP, Hanna SR. Modeling study of the aspect ratio influence on urban canopy energy fluxes with a modified wall-canyon energy budget scheme. Building and Environment, 2010, 45(11): 2497-2505.

[17] Song JY, Wang ZH. Interfacing the urban land–atmosphere system through coupled urban canopy and atmospheric models. Boundary-Layer Meteorology, 2015, 154(3): 427-448.

[18] Oke TR. Street design and urban canopy layer climate. Energy and Buildings, 1988, 11(1-3): 103-113.

[19] Toparlar Y, Blocken B, Maiheu B, van Heijst GJF. A review on the CFD analysis of urban microclimate. Renewable and Sustainable Energy Reviews, 2017, 80: 1613-1640.

[20] Yang XS, Yao LY, Jin T, Peng LLH, Jiang ZD, Hu ZY, Ye YH. Assessing the thermal behavior of different local climate zones in the Nanjing metropolis, China. Building and Environment, 2018, 137: 171-184.

[21] Stewart ID, Oke TR. Local climate zones for urban temperature studies. Bulletin

of the American Meteorological Society, 2012, 93(12): 1879-1900.

[22] Lin Y, Ichinose T, Yamao Y, Mouri H. Wind velocity and temperature fields under different surface heating conditions in a street canyon in wind tunnel experiments. Building and Environment, 2020, 168: 106500.

[23] Fan YF, Wang Q, Yin S, Li YG. Effect of city shape on urban wind patterns and convective heat transfer in calm and stable background conditions. Building and Environment, 2019, 162: 106288.

[24] Kanda M. Progress in the scale modeling of urban climate: review. Theoretical and Applied Climatology, 2006, 84(1-3): 23-33.

[25] Kawai T, Kanda M. Urban energy balance obtained from the comprehensive outdoor scale model experiment. Part I: basic features of the surface energy balance. Journal of Applied Meteorology and Climatology, 2010, 49(7): 1341-1359.

[26] Nottrott A, Onomura S, Inagaki A, Kanda M, Kleissl J. Convective heat transfer on leeward building walls in an urban environment: measurements in an outdoor scale model. International Journal of Heat and Mass Transfer, 2011, 54(15-16): 3128-3138.

[27] Kruger EL, Pearlmutter D. The effect of urban evaporation on building energy demand in an arid environment. Energy and Buildings, 2008, 40(11): 2090-2098.

[28] Park M, Hagishima A, Tanimoto J, Narita K. Effect of urban vegetation on outdoor thermal environment: field measurement at a scale model site. Building and Environment, 2012, 56: 38-46.

[29] Syafii NI, Ichinose M, Kumakura E, Jusuf SK, Chigusa K, Wong NH. Thermal environment assessment around bodies of water in urban canyons: a scale model study. Sustainable Cities and Society, 2017, 34: 79-89.

[30] Aida M. Urban albedo as a function of the urban structure–a model experiment. Boundary-Layer Meteorology, 1982, 23(4): 405-413.

[31] Pearlmutter D, Berliner P, Shaviv E. Physical modeling of pedestrian energy exchange within the urban canopy. Building and Environment, 2006, 41(6): 783-795.

[32] Wang K, Li YG, Luo ZW, Yin S, Chan PW. Harmonic analysis of 130-year hourly air temperature in Hong Kong: detecting urban warming from the perspective of annual and daily cycles. Climate Dynamics, 2018, 51(1-2): 613-625.

[33] Toparlar Y, Blocken B, Vos P, van Heijst GJF, Janssen WD, van Hooff T, Montazeri H, Timmermans HJP. CFD simulation and validation of urban microclimate: a case study for Bergpolder Zuid, Rotterdam. Building and Environment, 2015, 83: 79-90.

[34] Yang XY, Li YG, Luo ZW, Chan PW. The urban cool island phenomenon in a high-rise high-density city and its mechanisms. International Journal of Climatology, 2017, 37(2): 890-904.

[35] Chen GW, Wang DY, Wang Q, Li YG, Wang XM, Hang J, Gao P, Ou CY, Wang K. Scaled outdoor experimental studies of urban thermal environment in street canyon models with various aspect ratios and thermal storage. Science of the Total Environment, 2020, 726: 138147.

[36] Dai YW, Mak CM, Zhang Y, Cui DJ, Hang J. Investigation of interunit dispersion in 2D street canyons: a scaled outdoor experiment. Building and Environment, 2020, 171: 106673.

[37] Chen GW, Yang X, Yang HY, Hang J, Lin YY, Wang XM, Wang Q, Liu YL. The influence of aspect ratios and solar heating on flow and ventilation in 2D street canyons by scaled outdoor experiments. Building and Environment, 2020, 185: 107159.

[38] Chen TH, Yang HY, Chen GW, Lam CKC, Hang J, Wang XM, Liu YL, Ling H. Integrated impacts of tree planting and aspect ratios on thermal environment in street canyons by scaled outdoor experiments. Science of the Total Environment, 2020: 142920.

[39] Offerle B, Eliasson I, Grimmond CSB, Holmer B. Surface heating in relation to air temperature, wind and turbulence in an urban street canyon. Boundary-Layer Meteorology, 2007, 122(2): 273-292.

[40] Wang K, Li YG, Wang Y, Yang XY. On the asymmetry of the urban daily air temperature cycle. Journal of Geophysical Research: Atmospheres, 2017, 122(11): 5625-5635.

[41] Wang K, Li YG, Li YH, Lin BR. Stone forest as a small-scale field model for the study of urban climate. International Journal of Climatology, 2018, 38(9): 3723-3731.

[42] Louka P, Vachon G, Sini JF, Mestayer PG, Rosant JM. Thermal effects on the airflow in a street canyon–Nantes' 99 experimental results and model simulations. Water, Air and Soil Pollution: Focus, 2002, 2(5-6): 351-364.

[43] Hang J, Chen XY, Chen GW, Chen TH, Lin YY, Luo ZW, Zhang XL, Wang Q. The influence of aspect ratios and wall heating conditions on flow and passive pollutant exposure in 2D typical street canyons. Building and Environment, 2020, 168: 106536.

[44] Bourbia F, Awbi HB. Building cluster and shading in urban canyon for hot dry climate: part 2: shading simulations. Renewable Energy, 2004, 29(2): 291-301.

[45] Nunez M, Oke TR. The energy balance of an urban canyon. Journal of Applied Meteorology, 1977, 16(1): 11-19.

[46] Johansson E. Influence of urban geometry on outdoor thermal comfort in a hot dry climate: a study in Fez, Morocco. Building and Environment, 2006, 41(10): 1326-1338.

[47] Georgakis C, Santamouris M. Experimental investigation of air flow and temperature distribution in deep urban canyons for natural ventilation purposes. Energy and Buildings, 2006, 38(4): 367-376.

[48] Harman IN, Best MJ, Belcher SE. Radiative exchange in an urban street canyon. Boundary-Layer Meteorology, 2004, 110(2): 301-316.

[49] Gros A, Bozonnet E, Inard C, Musy M. Simulation tools to assess microclimate and building energy–a case study on the design of a new district. Energy and Buildings, 2016, 114: 112-122.

[50] Grimmond CSB, Blackett M, Best MJ, Barlow J, Baik JJ, Belcher SE, Bohnenstengel SI, Calmet I, Chen F, Dandou A, Fortuniak K, Gouvea ML, Hamdi R, Hendry M, Kawai T, Kawamoto Y, Kondo H, Krayenhoff ES, Lee SH, Loridan T, Martilli A, Masson V, Miao S, Oleson K, Pigeon G, Porson A, Ryu YH, Salamanca F, Shashua-Bar L, Steeneveld GJ, Tombrou M, Voogt J, Young D, Zhang N. The international urban energy balance models comparison project: first results from phase 1. Journal of Applied Meteorology and Climatology, 2010, 49(6): 1268-1292.

[51] Schrijvers PJC, Jonker HJJ, de Roode SR, Kenjeres S. On the daytime micro-climatic conditions inside an idealized 2D urban canyon. Building and Environment, 2020, 167: 106427.

[52] Yang XY, Li YG. Development of a three-dimensional urban energy model for predicting and understanding surface temperature distribution. Boundary-Layer Meteorology, 2013, 149(2): 303-321.

[53] Ryu YH, Baik JJ, Lee SH. A new single-layer urban canopy model for use in mesoscale atmospheric models. Journal of Applied Meteorology and Climatology, 2011, 50(9): 1773-1794.

[54] Sparrow EM, Cess RD. Radiation heat transfer, 1978, Chapter 3-4.

[55] Duffie JA, Beckman WA. Solar engineering of thermal processes. John Wiley & Sons, 2013, Chapter 1.

[56] Kalogirou SA. Solar energy engineering: processes and systems. Academic Press, 2013, Chapter 2.

[57] Reindl DT, Beckman WA, Duffie JA. Diffuse fraction correlations. Solar energy, 1990, 45(1): 1-7.

[58] Offerle B, Grimmond CSB, Fortuniak K. Heat storage and anthropogenic heat flux in relation to the energy balance of a central European city centre. International Journal of Climatology, 2005, 25(10): 1405-1419.

[59] Lee DI, Lee SH. The microscale urban surface energy (MUSE) model for real urban application. Atmosphere, 2020, 11(12):1347.

[60] Rowley FB, Algren AB, Blackshaw JL. Surface conductances as affected by air velocity, temperature and character of surface. ASHRAE Trans, 1930, 36: 429-446.

Table 1. Physical properties of canyon model material.

Material	Density, ρ (g/cm^3)	Conductivity, k (W/mK)	Diffusivity, D (mm^2/s)	Volumetric heat capacity, C (MJ/m^3K)	Emissivity, ε	Albedo, α
Concrete	2.42	2.073	1.386	1.496	0.87	0.24

Table 2. Specifications and configurations of instrument used in this measurement (the vertical postion is relative to the ground).

Measured parameter	Instrument	Accuracy	Horizontal position	Vertical position	Sampling rate	Quantity
Background air temperature, rainfall, relative humidity	Weather station (RainWise PortLog)	0.5 ℃ in the range of -54 ～ 65 ℃, 2 % at 25.4 mm/h, 2 % from -40 ℃ to 65 ℃		2.4 m	5 min	2
Global solar radiation	CMP10 (Kipp & Zonen)	0.2 % in the range of 100 ～ 1000 W/m^2		1.3 m	1 s	1
Downward longwave radiation	CGR3 (Kipp & Zonen)	1 % in the range of -250 ～ 250 W/m^2		1.9 m	1 s	1
East and west wall temperature	Thermocouple (Omega, TT-K-30-SLE, Φ0.255 mm)	1.1 ℃ or 0.4 % in the range of -200 ～ 260 °C, refer to the greater one	Refer to Fig. 1b	Refer to Fig. 2a-b	3 s	200
Canyon air temperature	Thermocouple (Omega, TT-K-36-SLE, Φ0.127 mm)	1.1 ℃ or 0.4 % in the range of -200 ～ 260 °C, refer to the greater one		Refer to Fig. 3a-c	3 s	198
Ground temperature	Thermocouple (Omega, TT-K-36-SLE, Φ0.127 mm)	1.1 ℃ or 0.4 % in the range of -200 ～ 260 °C, refer to the greater one		Refer to Fig. 4	3 s	21
Wind velocity	Sonic anemometer (Gill WindMaster)	1.5 % in the range of 0 ～ 50 m/s, 2° in the range of 0 ～ 359.9°		Refer to Fig. 5	20 Hz	6

Table 3. Summary of the normalized velocity magnitude $V_{0.25H}/V_{2H}$ in street canyons with various aspect ratios (H/W = 1, 2, 3) during the entire experimental period. The coefficient of determination (R^2) is used to evaluate the goodness of fit.

Aspect ratio	$H/W = 1$	$H/W = 2$	$H/W = 3$
$V_{0.25H}/V_{2H}$	0.41	0.36	0.21
R^2	0.94	0.95	0.93

Table 4. Summary of the root mean squared error (RMSE) between the Q_H and $Q_{H_{res}}$

Aspect ratio	$H/W = 1$	$H/W = 2$	$H/W = 3$
RMSE (W/m^2)	60.7	32.4	23.0

Table 5. Summary of the spatially averaged values with standard deviations of diurnal temperature characteristics at all corresponding points of canyon air, west, and east wall, including the daily average temperature $\overline{T}$ (°C), daily temperature range (DTR) (°C), and hottest time t_{max} (h).

Aspect ratio (H/W)	Canyon element	$\overline{T}$	DTR	$t_{\max}$
0.5	Canyon air	24.3 ± 0.6	10.9 ± 1.2	13.85 ± 0.15
	West wall	27.9 ± 0.2	18.5 ± 2.2	13.13 ± 0.09
	East wall	28.7 ± 0.4	26.1 ± 2.9	14.17 ± 0.10
1	Canyon air	24.2 ± 0.3	10.4 ± 1.1	14.03 ± 0.14
	West wall	26.7 ± 0.3	16.0 ± 1.9	13.96 ± 0.07
	East wall	27.5 ± 0.8	22.8 ± 4.0	14.47 ± 0.20
2	Canyon air	24.3 ± 0.4	10.3 ± 1.2	14.00 ± 0.11
	West wall	26.4 ± 0.3	14.6 ± 2.6	14.03 ± 0.19
	East wall	26.9 ± 1.0	18.4 ± 5.6	14.32 ± 0.15
3	Canyon air	24.5 ± 0.5	10.3 ± 1.1	14.00 ± 0.09
	West wall	26.1 ± 0.6	13.8 ± 3.8	14.28 ± 0.33
	East wall	26.6 ± 1.1	16.5 ± 7.0	14.45 ± 0.15
6	Canyon air	24.6 ± 0.3	9.3 ± 1.6	14.25 ± 0.22
	West wall	26.6 ± 1.1	11.7 ± 4.7	14.85 ± 0.65
	East wall	26.3 ± 1.0	12.9 ± 6.6	15.09 ± 0.56

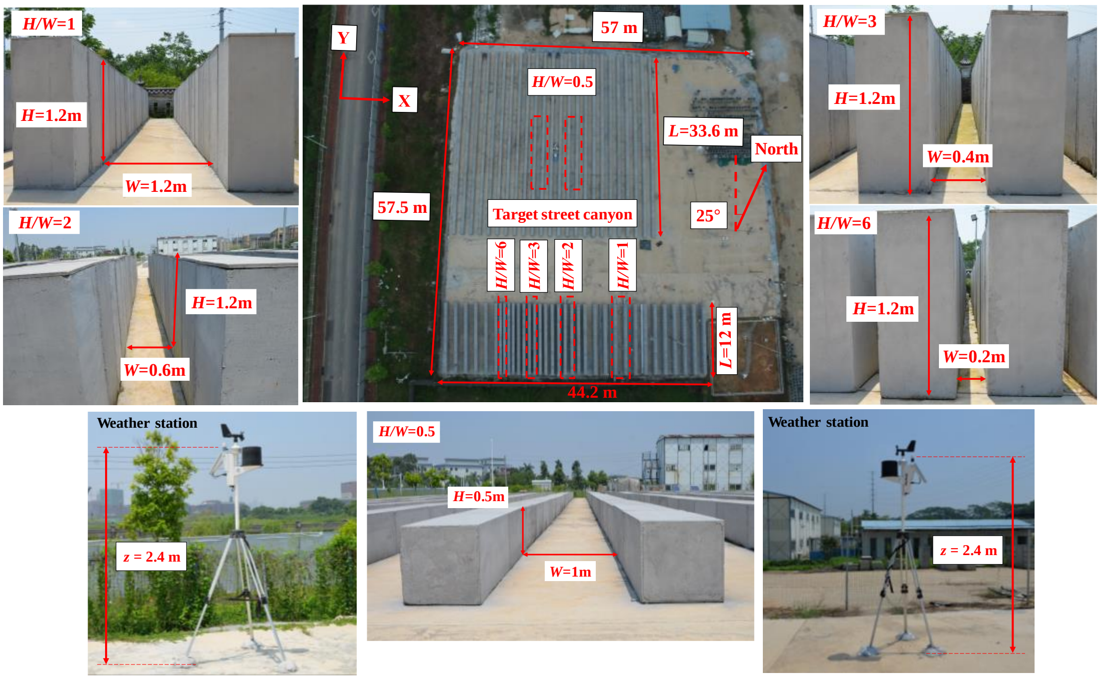
H/W=1
H=1.2m
W=1.2m
H/W=2
H=1.2m
W=0.6m
Y
X
57 m
H/W=0.5
L=33.6 m
North
57.5 m
Target street canyon
25°
H/W=6
H/W=3
H/W=2
H/W=1
L=12 m
44.2 m
H/W=3
H=1.2m
W=0.4m
H/W=6
H=1.2m
W=0.2m
Weather station
z = 2.4 m
H/W=0.5
H=0.5m
W=1m
Weather station
z = 2.4 m

(a)

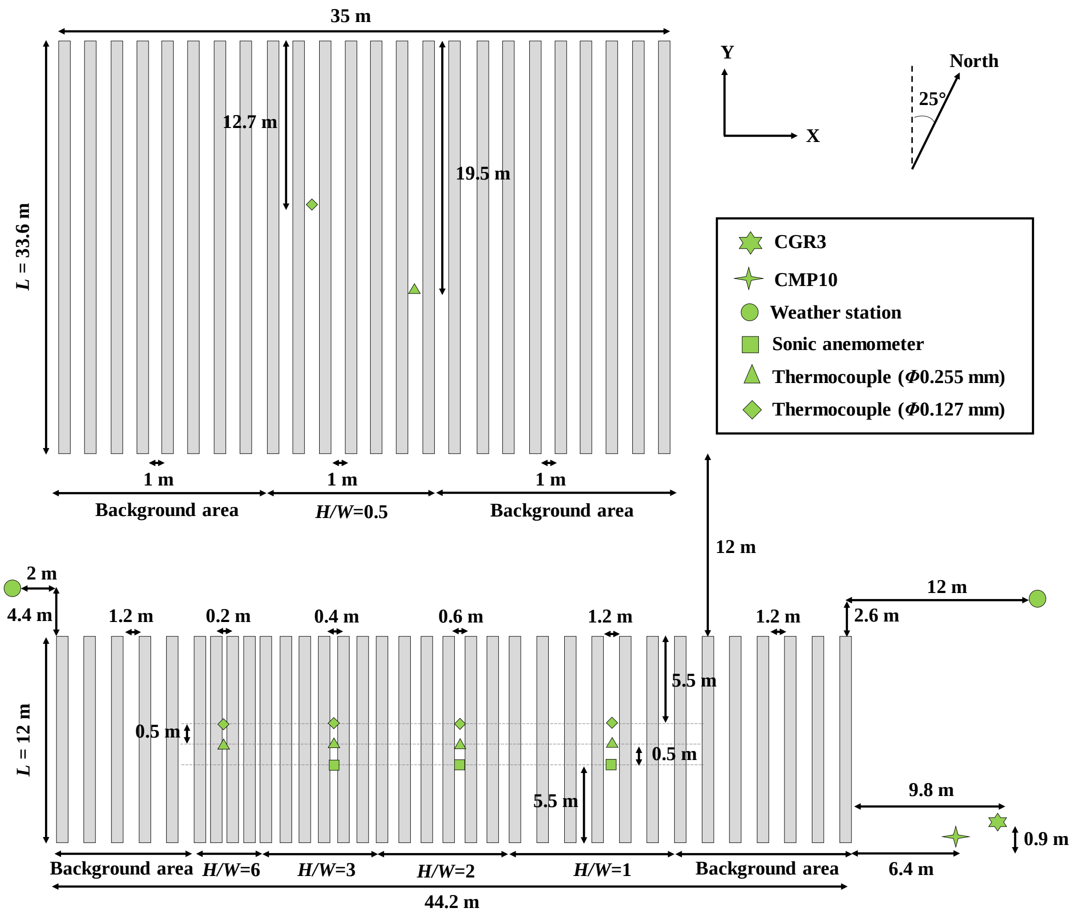
35 m
12.7 m
19.5 m
L = 33.6 m
Y
X
North
25°
CGR3
CMP10
Weather station
Sonic anemometer
Thermocouple (Φ0.255 mm)
Thermocouple (Φ0.127 mm)
1 m
1 m
1 m
Background area
H/W=0.5
Background area
12 m
2 m
4.4 m
1.2 m
0.2 m
0.4 m
0.6 m
1.2 m
1.2 m
12 m
2.6 m
5.5 m
L = 12 m
0.5 m
0.5 m
5.5 m
9.8 m
0.9 m
Background area
H/W=6
H/W=3
H/W=2
H/W=1
Background area
6.4 m
44.2 m

(b)

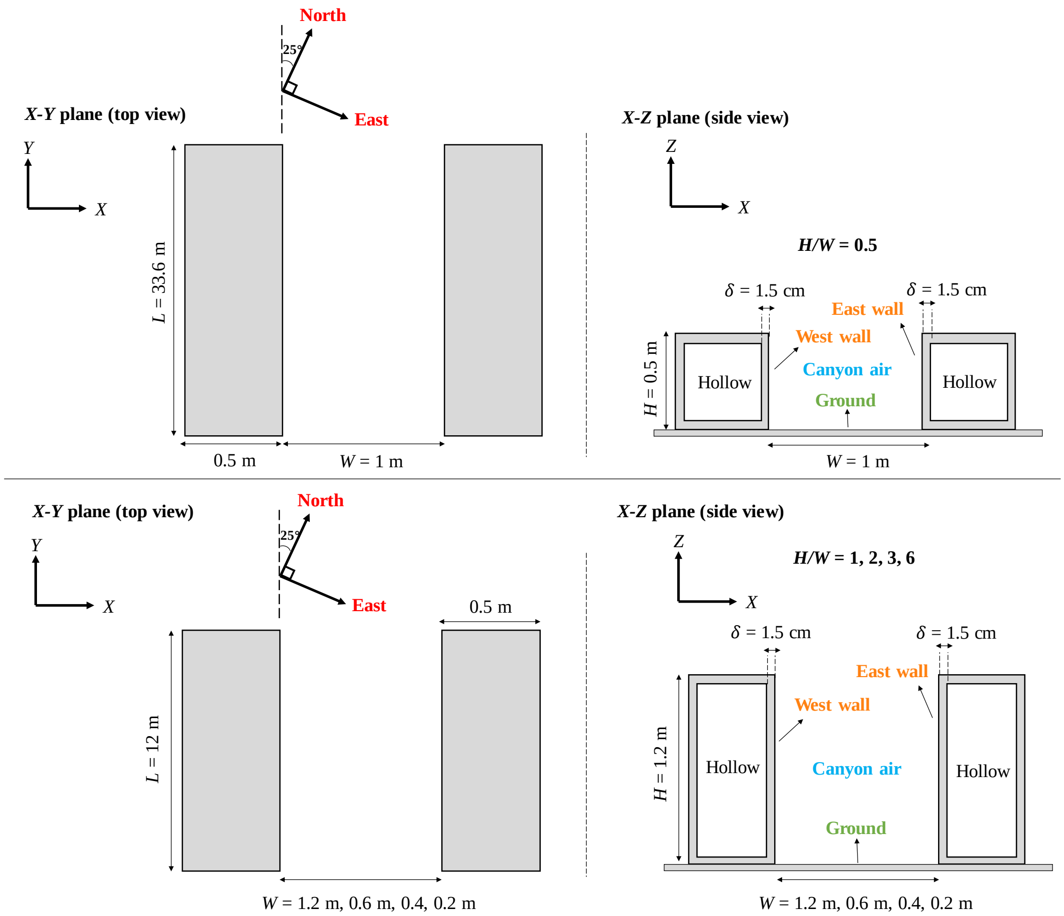

(c)

Fig. 1 (a) Overview of the experiment site; Schematic illustrations of: (b) the measurement positions within street canyons with various aspect ratios (*H*/*W* = 0.5, 1, 2, 3, 6) in *X*-*Y* plane (top view), (c) the definitions of the canyon air, ground, east wall, and west wall inside street canyons in *X*-*Y* plane (top view) and *X*-*Z* plane (side view).

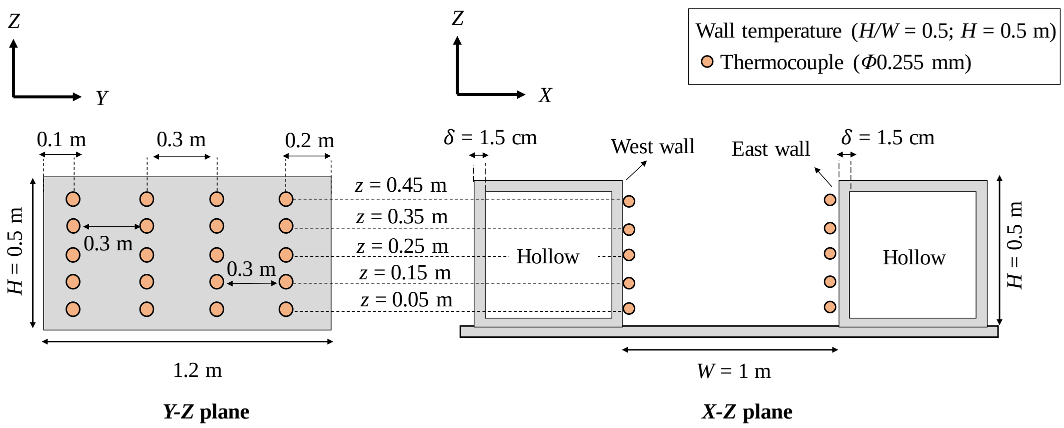

(a)

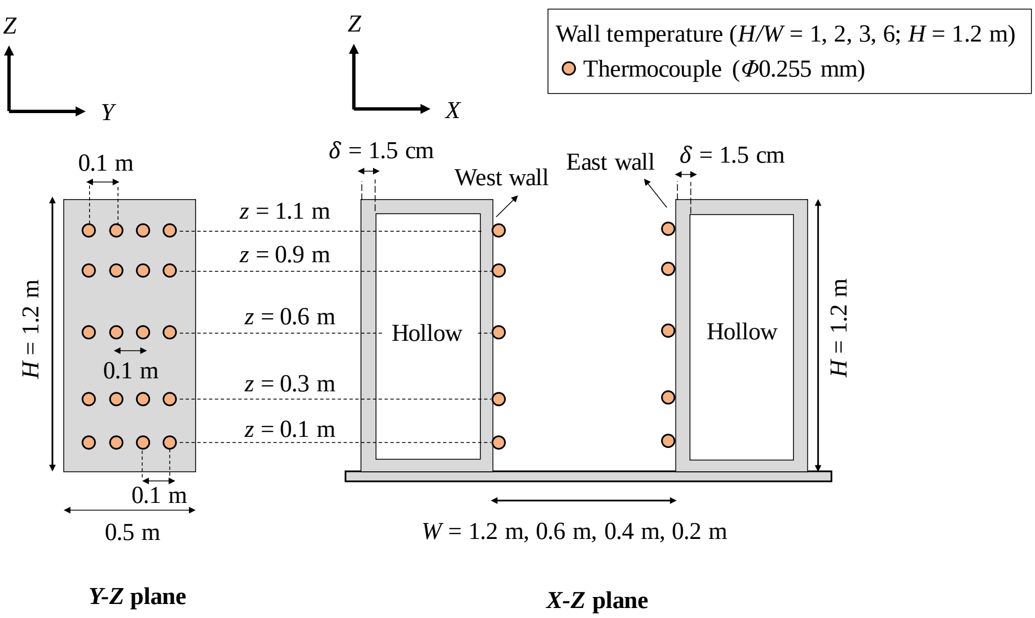

(b)

Fig. 2 Schematic setup of the west and east wall temperature measured by thermocouples (Omega, TT-K-30-SLE, Φ0.255 mm) in *X*-*Z* plane and *Y*-*Z* plane: (a) $H/W = 0.5$, $H = 0.5$ m; (b) $H/W = 1, 2, 3, 6$, $H = 1.2$ m.

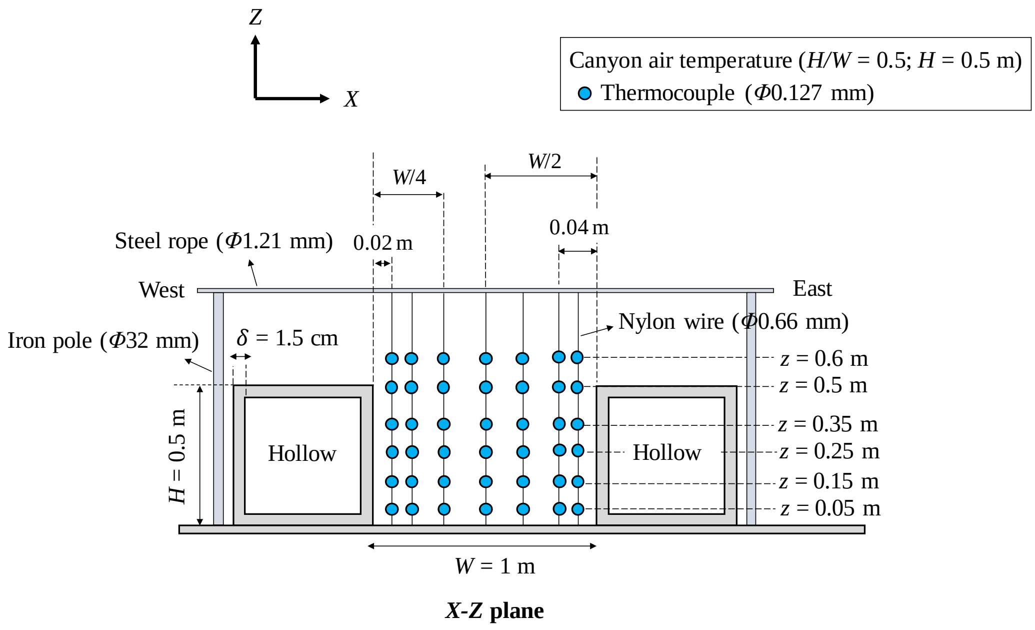
Z
X
Canyon air temperature (H/W = 0.5; H = 0.5 m)
Thermocouple (Φ0.127 mm)
W/4
W/2
0.04 m
Steel rope (Φ1.21 mm)
0.02 m
West
East
Nylon wire (Φ0.66 mm)
Iron pole (Φ32 mm)
δ = 1.5 cm
z = 0.6 m
z = 0.5 m
z = 0.35 m
z = 0.25 m
z = 0.15 m
z = 0.05 m
H = 0.5 m
Hollow
Hollow
W = 1 m
X-Z plane

(a)

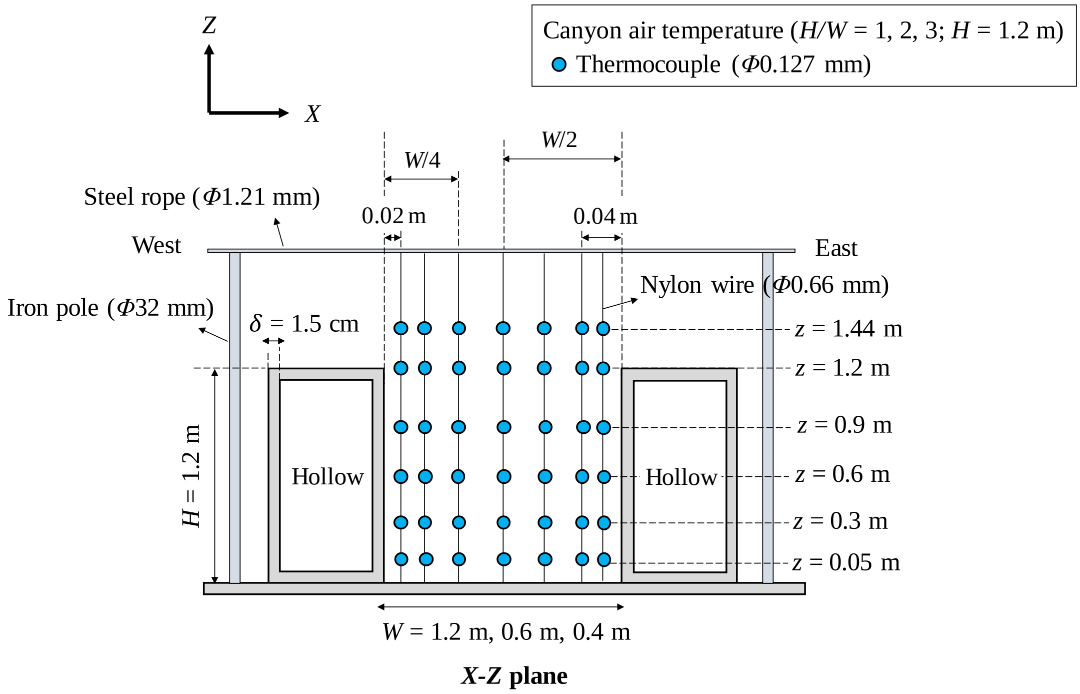
Z
X
Canyon air temperature (H/W = 1, 2, 3; H = 1.2 m)
Thermocouple (Φ0.127 mm)
W/2
W/4
Steel rope (Φ1.21 mm)
0.02 m
0.04 m
West
East
Nylon wire (Φ0.66 mm)
Iron pole (Φ32 mm)
δ = 1.5 cm
z = 1.44 m
z = 1.2 m
z = 0.9 m
z = 0.6 m
z = 0.3 m
z = 0.05 m
H = 1.2 m
Hollow
Hollow
W = 1.2 m, 0.6 m, 0.4 m
X-Z plane

(b)

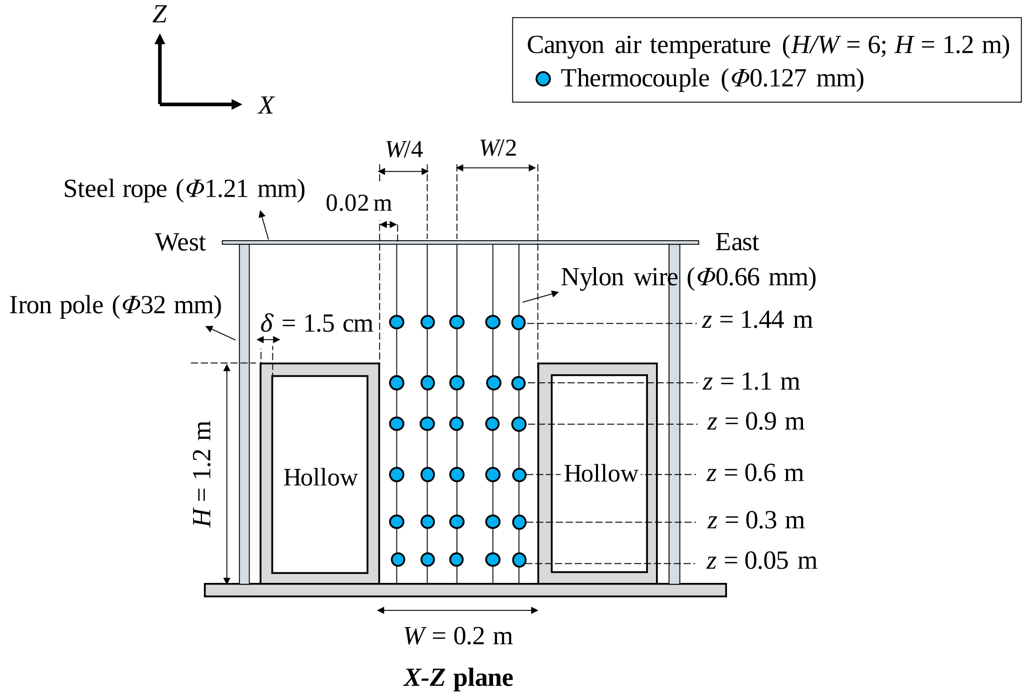

(c)

Fig. 3 Schematic setup of the canyon air temperature measured by thermocouples (Omega, TT-K-36-SLE, Φ0.127 mm) in X-Z plane: (a) H/W = 0.5, H = 0.5 m; (b) H/W = 1, 2, 3, H = 1.2 m; (c) H/W = 6, H = 1.2 m.

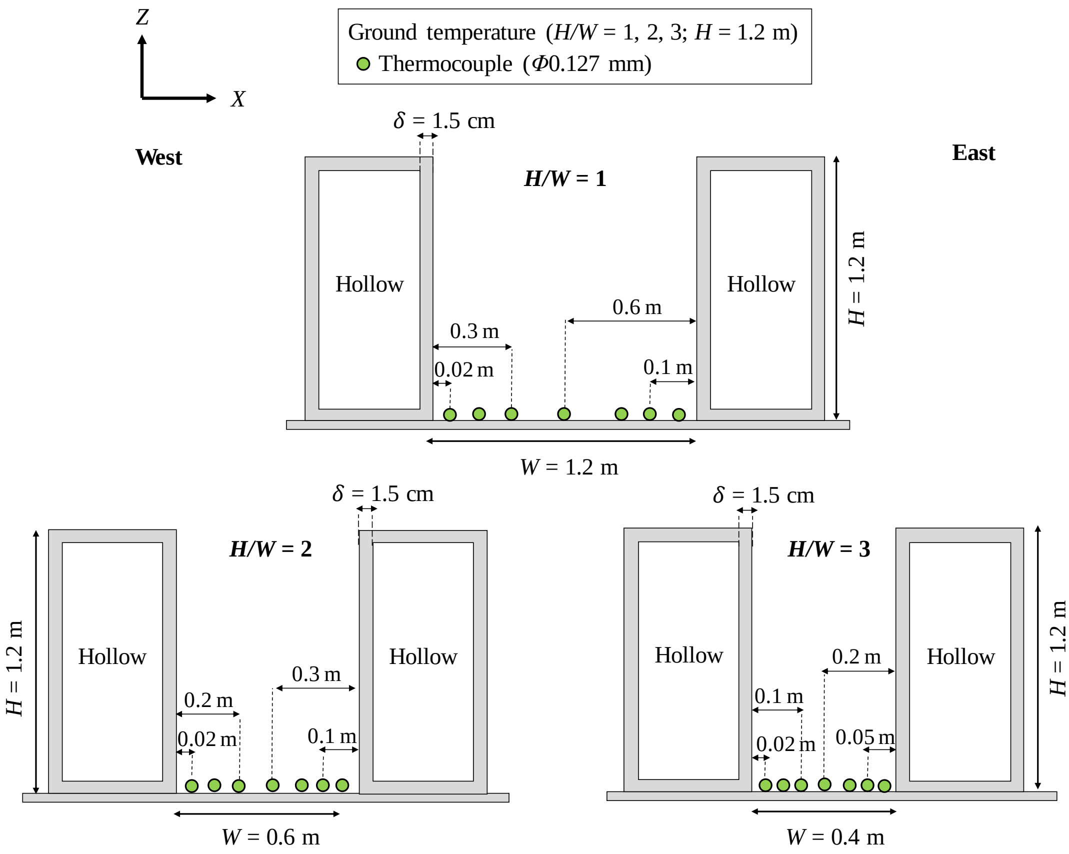

Fig. 4 Schematic setup of the ground temperature measured by thermocouples (Omega, TT-K-36-SLE, Φ0.127 mm) in X-Z plane: H/W = 1, 2, 3, H = 1.2 m.

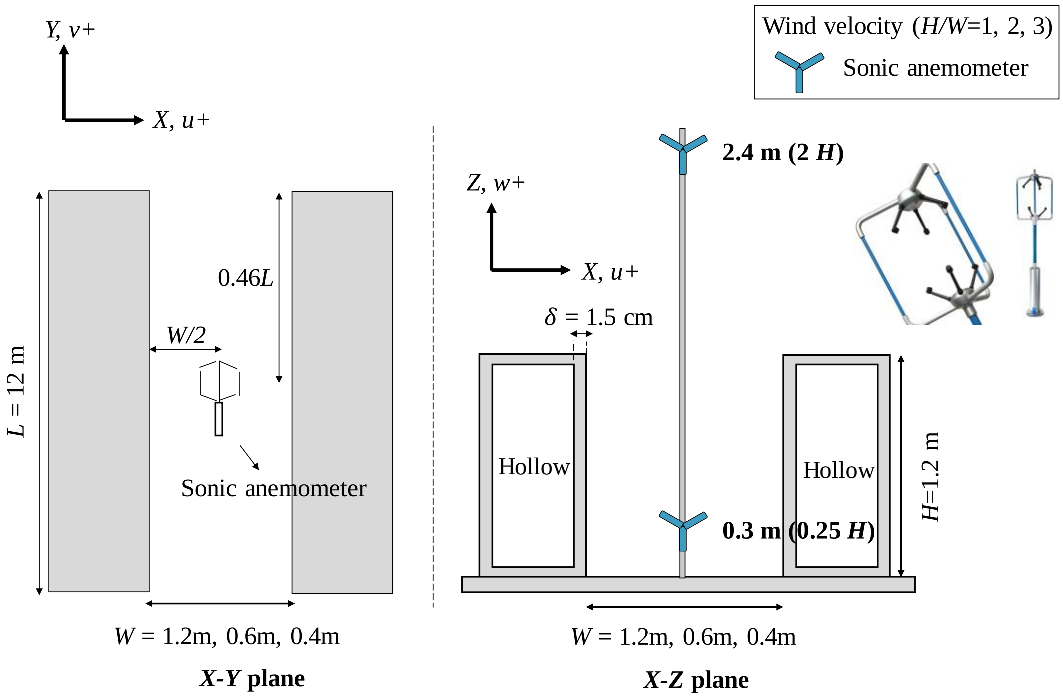

Fig. 5 Schematic setup of the sonic anemometers in street canyons with various aspect ratios (*H/W* = 1, 2, 3), in *X-Y* plane and *X-Z* plane.

942

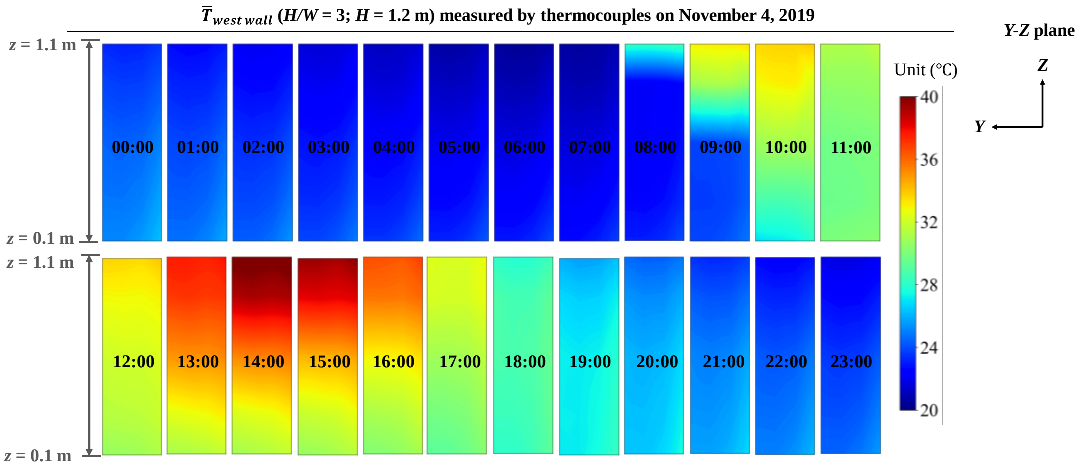

(a)

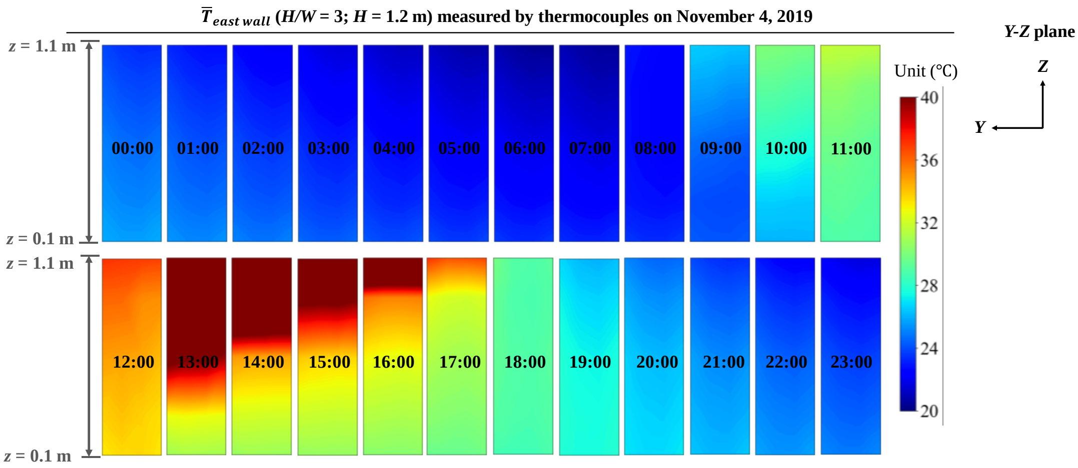

(b)

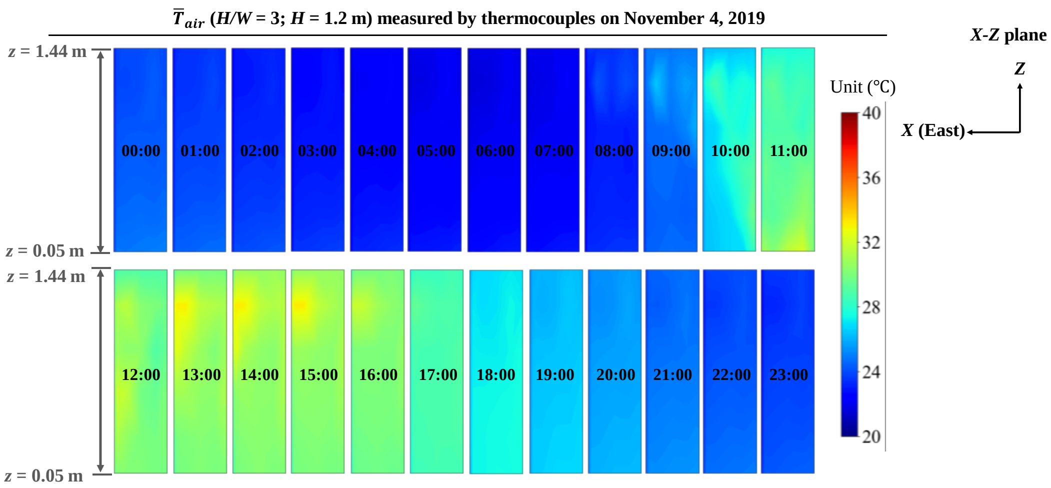

(c)

Fig. 6 Diurnal cycle of the linearly interpolated temperature distribution: (a)

$\overline{T}_{west\ wall}$; (b) $\overline{T}_{east\ wall}$; (c) $\overline{T}_{air}$.

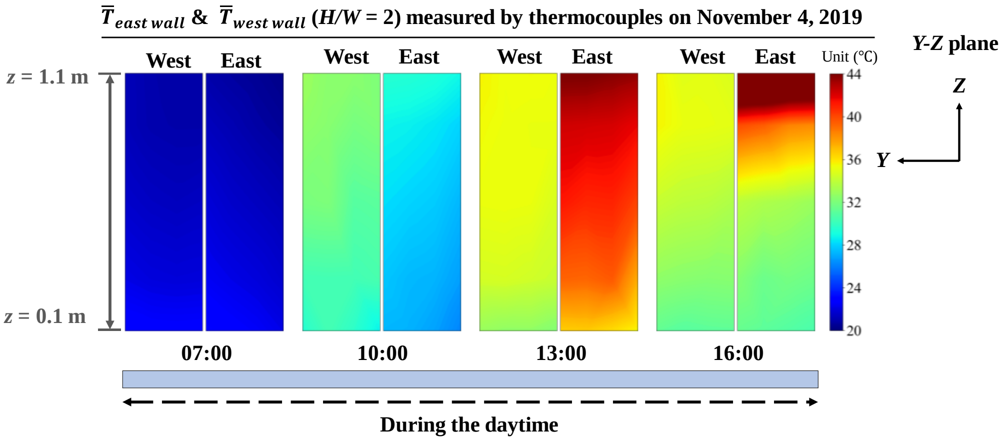

(a)

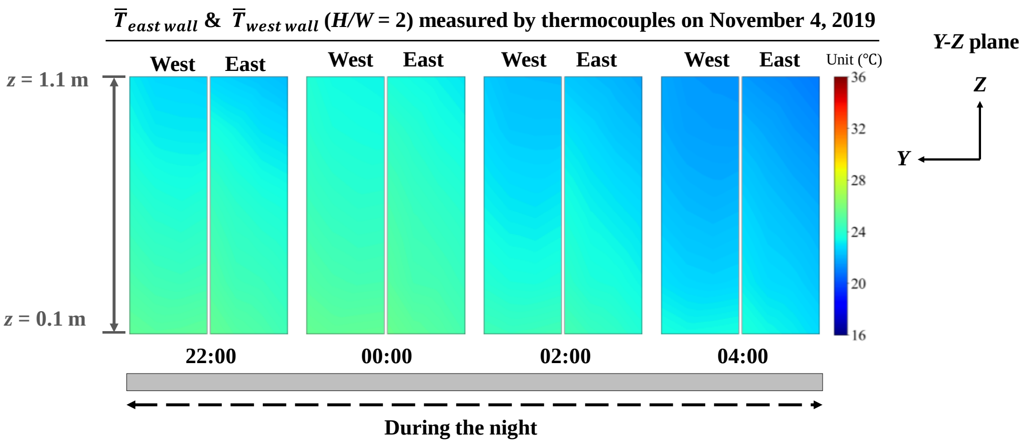

(b)

Fig. 7 Examples of the linearly interpolated temperature of west wall ($\overline{T}_{west\ wall}$), and east wall ($\overline{T}_{east\ wall}$): (a) during the daytime; (b) at night.

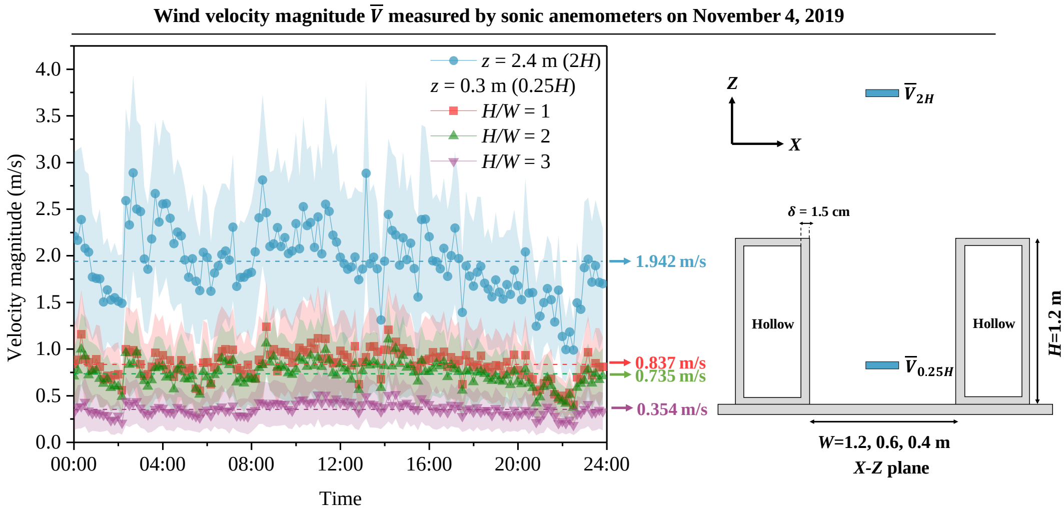

Fig. 8 Diurnal cycle of 10 min averaged wind velocity magnitude $\overline{V}$ and its standard deviation (as shown in the colored strips)

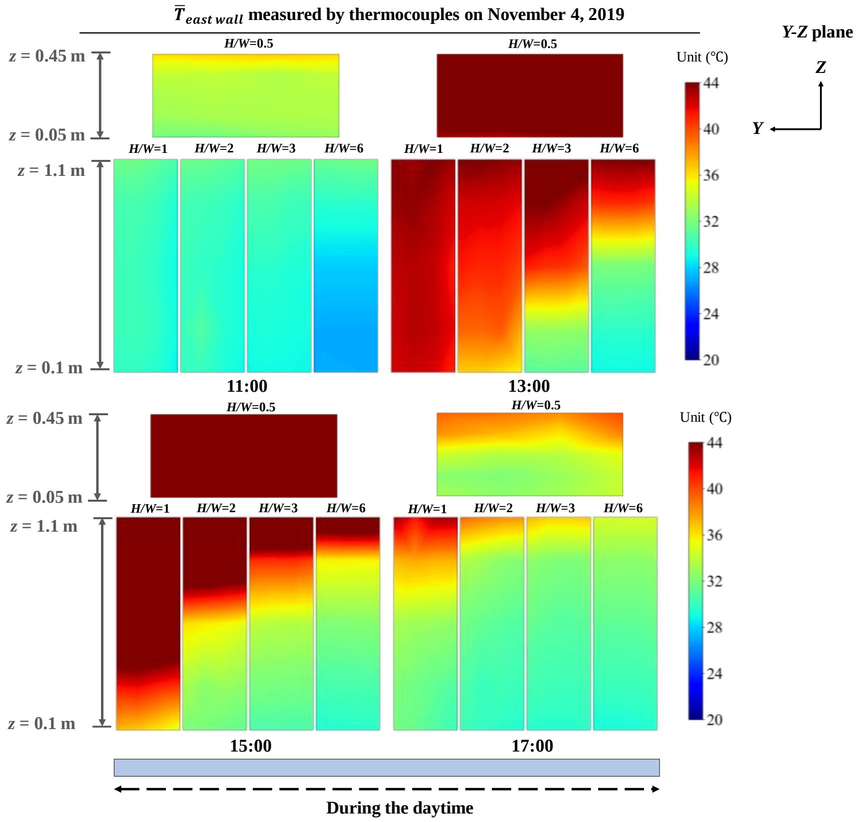

$\overline{T}_{east\ wall}$ measured by thermocouples on November 4, 2019
Y-Z plane
Z
Y
Unit (°C)
44
40
36
32
28
24
20
z = 0.45 m
z = 0.05 m
z = 1.1 m
z = 0.1 m
H/W=0.5
H/W=1
H/W=2
H/W=3
H/W=6
11:00
13:00
15:00
17:00
During the daytime

(a)

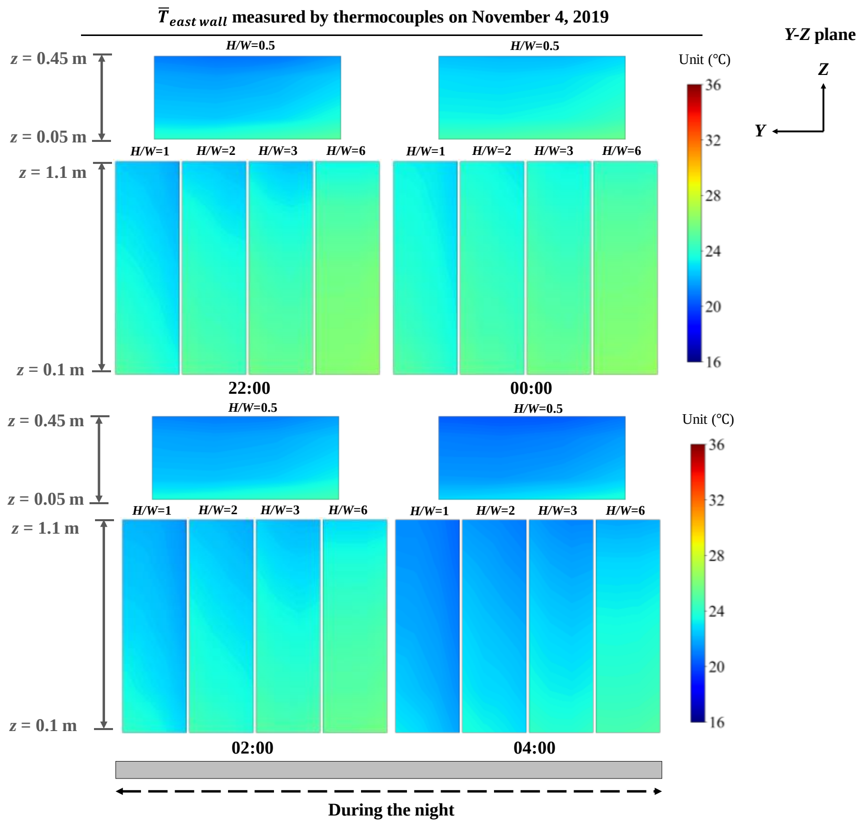

$\overline{T}_{east\ wall}$ measured by thermocouples on November 4, 2019
Y-Z plane
Z
Y
Unit (°C)
36
32
28
24
20
16
z = 0.45 m
z = 0.05 m
z = 1.1 m
z = 0.1 m
H/W=0.5
H/W=1
H/W=2
H/W=3
H/W=6
22:00
00:00
02:00
04:00
During the night

(b)

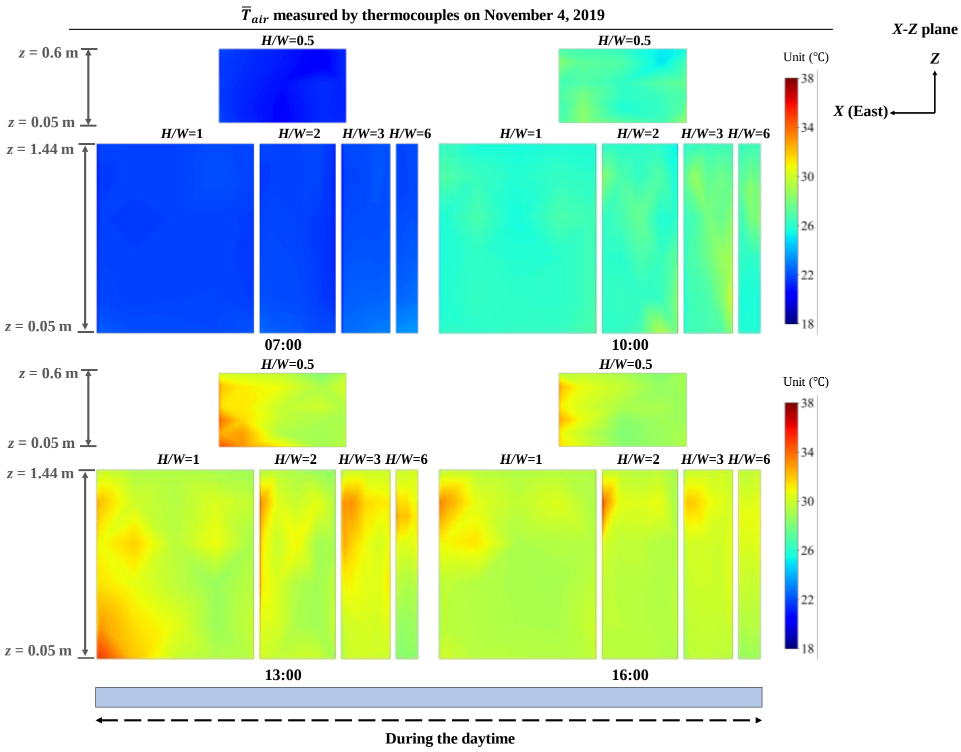

(c)

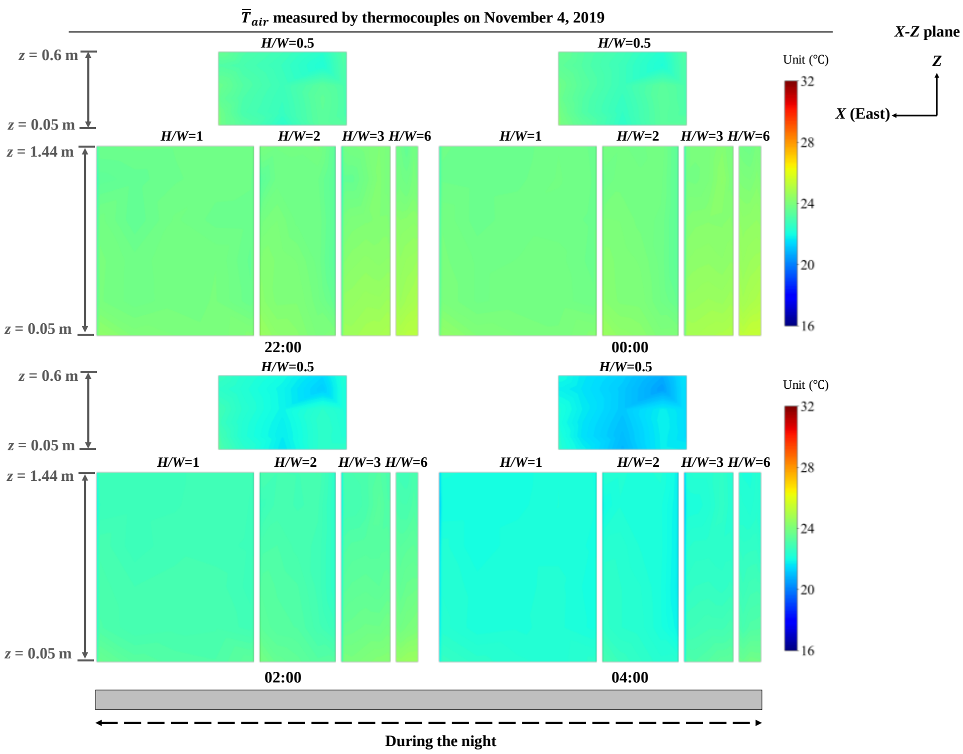

(d)

Fig. 9 Examples of the linearly interpolated temperature distribution in street canyons with five aspect ratios (*H/W* = 0.5, 1, 2, 3, 6): (a) during the daytime, $\overline{T}_{east\ wall}$; (b) at night, $\overline{T}_{east\ wall}$; (c) during the daytime, $\overline{T}_{air}$; (d) at night, $\overline{T}_{air}$.

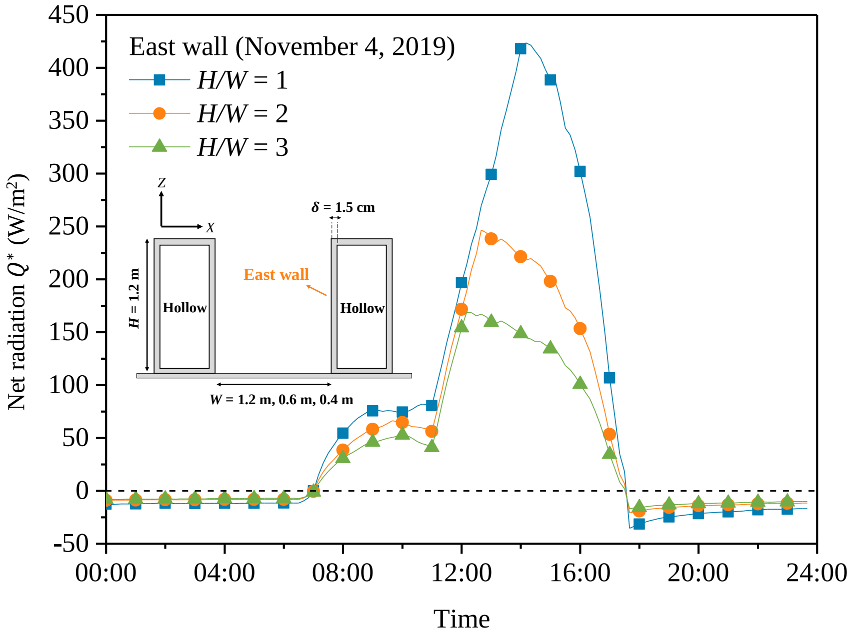
East wall (November 4, 2019)
H/W = 1
H/W = 2
H/W = 3
Net radiation Q* (W/m²)
Time
Hollow
Hollow
East wall
H = 1.2 m
δ = 1.5 cm
W = 1.2 m, 0.6 m, 0.4 m
z
x

(a)

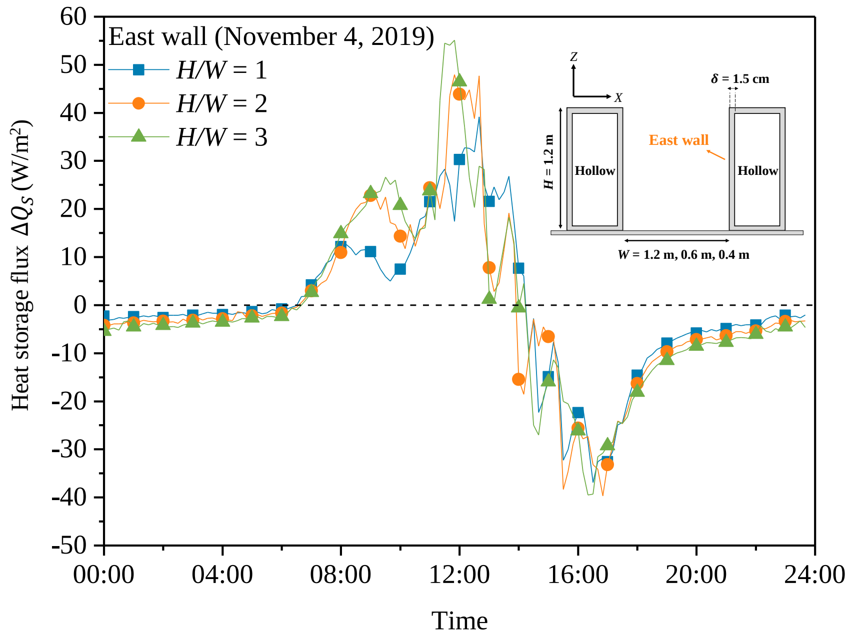
East wall (November 4, 2019)
H/W = 1
H/W = 2
H/W = 3
Heat storage flux ΔQS (W/m²)
Time
Hollow
Hollow
East wall
H = 1.2 m
δ = 1.5 cm
W = 1.2 m, 0.6 m, 0.4 m
z
x

(b)

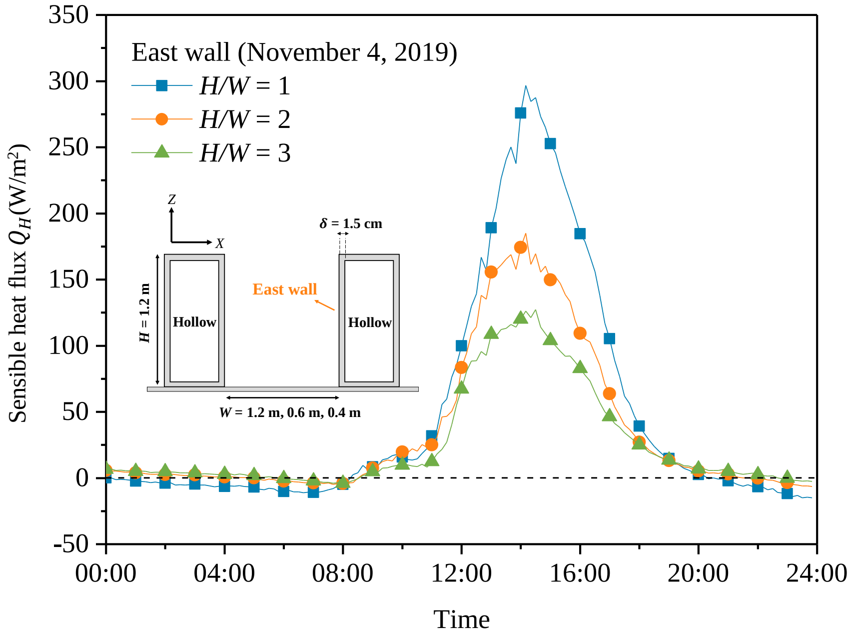

(c)

Fig. 10 Diurnal variations of the estimated heat fluxes (10 min averaged) of the east wall inside street canyons of *H/W* = 1, 2, 3: (a) net radiation, Q^*; (b) heat storage flux, ΔQ_S; (c) sensible heat flux, Q_H.

⟨$T_{west\ wall}$⟩ obtained from FFT measured by thermocouples during July 30-December 15, 2019

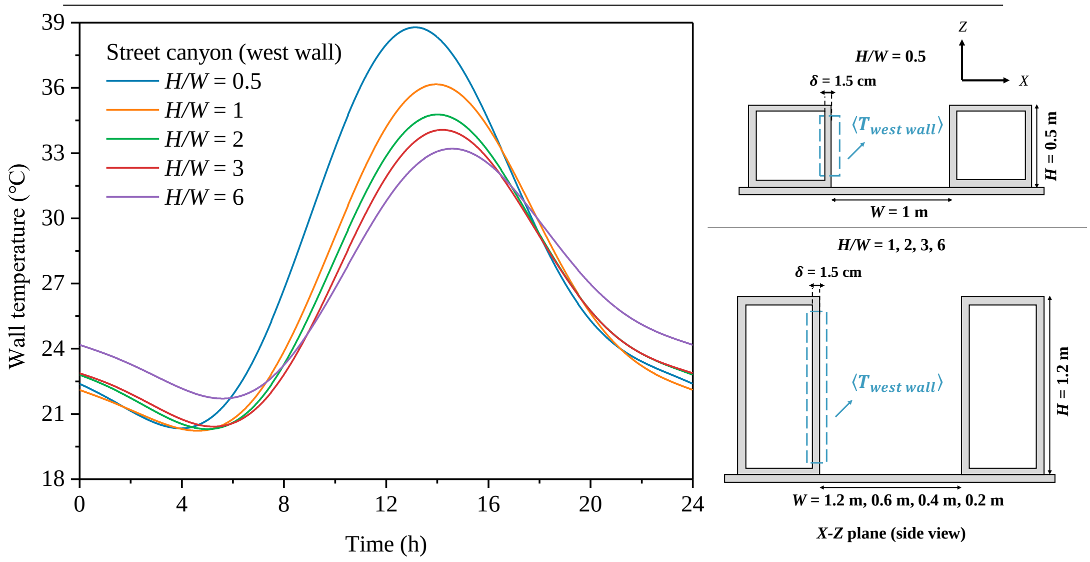

(a)

⟨$T_{east\ wall}$⟩ obtained from FFT measured by thermocouples during July 30-December 15, 2019

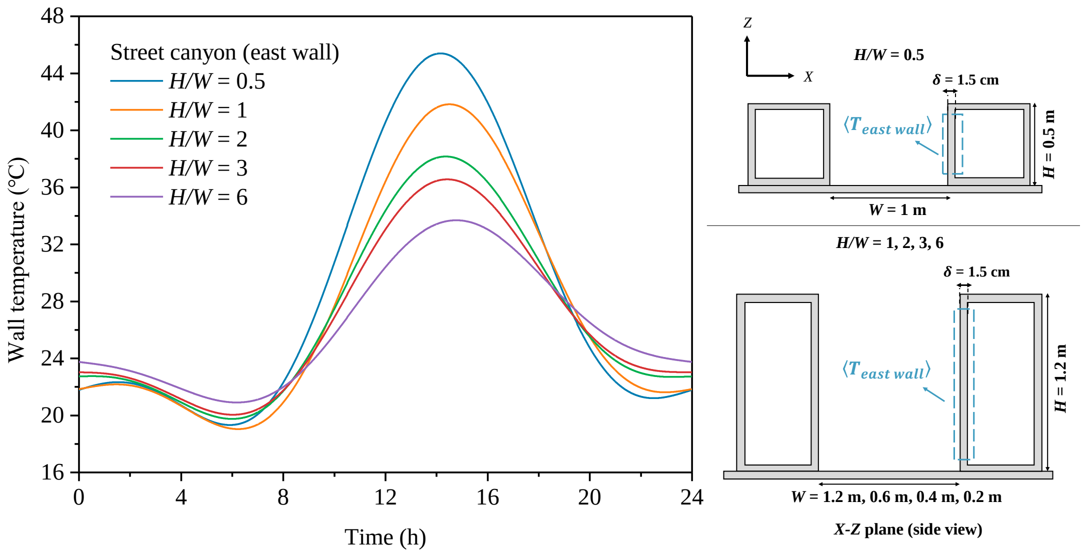

(b)

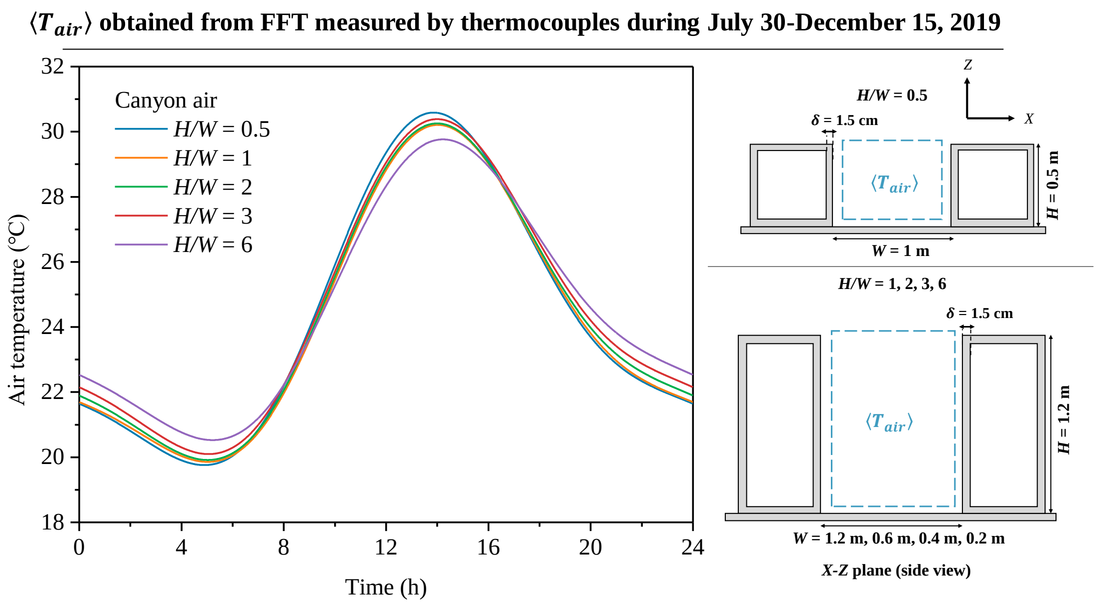

(c)

Fig. 11 Diurnal cycles of the spatially averaged temperature inside street canyons with various aspect ratios (*H/W* = 0.5, 1, 2, 3, 6): (a) west wall, $\langle T_{west\ wall}\rangle$; (b) east wall, $\langle T_{east\ wall}\rangle$; (c) canyon air, $\langle T_{air}\rangle$.

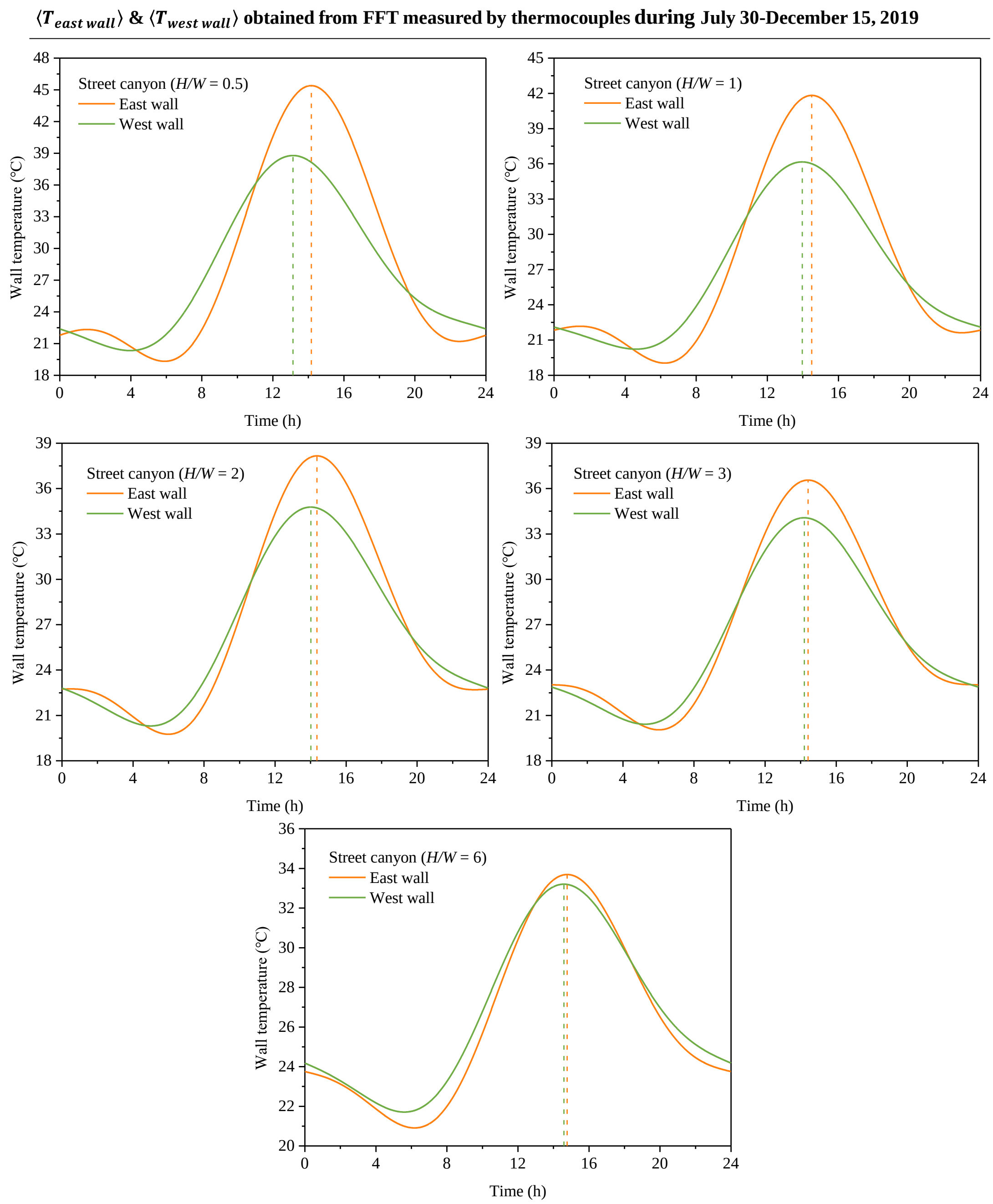

Fig. 12 Daily variations of the spatially averaged temperature of west wall (⟨$T_{west\ wall}$⟩), and east wall (⟨$T_{east\ wall}$⟩) in street canyons with different aspect ratios (*H/W* = 0.5, 1, 2, 3, 6).

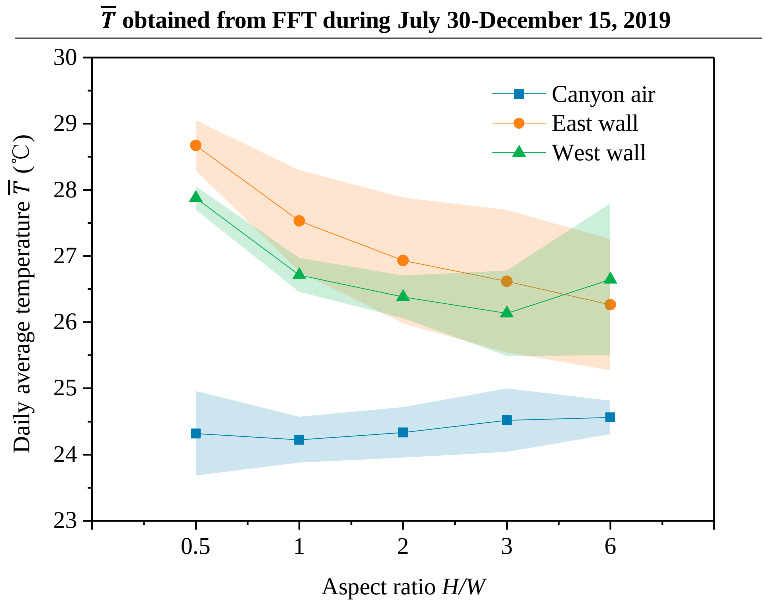
$\overline{T}$ obtained from FFT during July 30-December 15, 2019
Canyon air
East wall
West wall
Daily average temperature $\overline{T}$ (℃)
30
29
28
27
26
25
24
23
0.5
1
2
3
6
Aspect ratio H/W

(a)

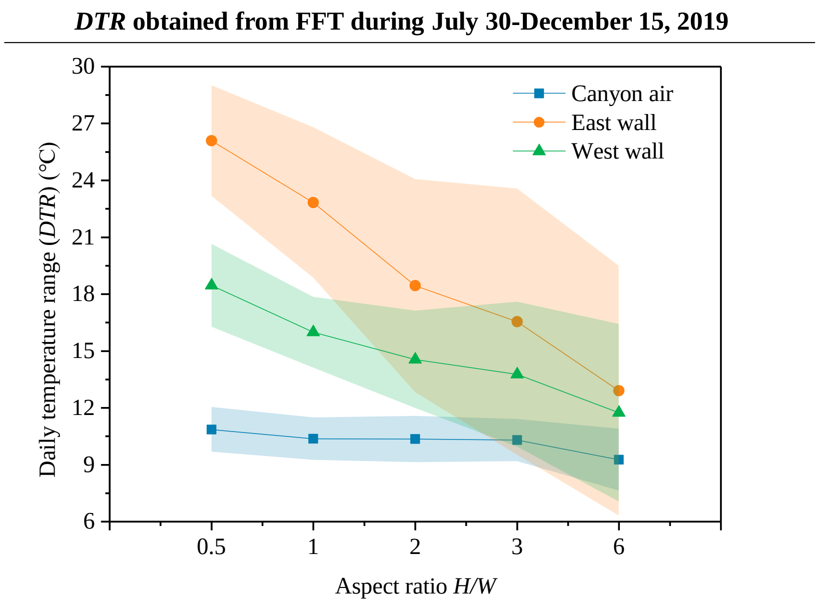
DTR obtained from FFT during July 30-December 15, 2019
Canyon air
East wall
West wall
Daily temperature range (DTR) (°C)
30
27
24
21
18
15
12
9
6
0.5
1
2
3
6
Aspect ratio H/W

(b)

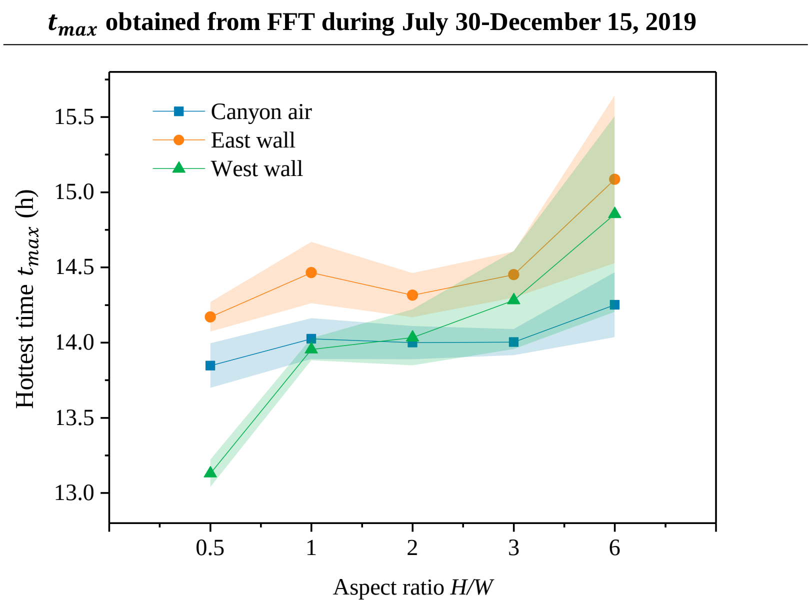

(c)

Fig. 13 Spatially averaged values with standard deviations (as shown in the colored strips) of the diurnal temperature characteristics at all corresponding points of canyon air, east wall, and west wall: (a) daily average temperature, $\overline{T}$; (b) daily temperature range, *DTR*; (c) hottest time, t_{max}.